

# GEOLOGIC MAP OF THE MCKENNA AND NORTHERN HALF OF THE LAKE LAWRENCE 7.5-MINUTE QUADRANGLES, THURSTON AND PIERCE COUNTIES, WASHINGTON

by Michael Polenz, Frank R. Hladky, Megan L. Anderson,  
Katherine A. Alexander, Jeffrey H. Tepper, Daniel P. Miggins,  
and Gabriel Legoretta Paulín

WASHINGTON  
GEOLOGICAL SURVEY

Map Series 2022-06

December 2022 [Revised March 2023]

INTERNALLY REVIEWED



WASHINGTON STATE DEPARTMENT OF

**NATURAL RESOURCES**

WASHINGTON GEOLOGICAL SURVEY



# GEOLOGIC MAP OF THE MCKENNA AND NORTHERN HALF OF THE LAKE LAWRENCE 7.5-MINUTE QUADRANGLES, THURSTON AND PIERCE COUNTIES, WASHINGTON

---

by Michael Polenz, Frank R. Hladky, Megan L. Anderson, Katherine A. Alexander, Jeffrey H. Tepper, Daniel P. Miggins, and Gabriel Legoretta Paulín

WASHINGTON  
GEOLOGICAL SURVEY  
Map Series 2022-06  
December 2022 [Revised March 2023]

*This geologic map was funded in part by  
the USGS National Cooperative Geologic  
Mapping Program, award no. G20AC00247*

*This publication has been subject to an iterative technical review  
process by at least one Survey geologist who is not an author.  
This publication has also been subject to an iterative  
review process with Survey editors and cartographers.*



WASHINGTON STATE DEPARTMENT OF  
**NATURAL RESOURCES**  
WASHINGTON GEOLOGICAL SURVEY

## DISCLAIMER

Neither the State of Washington, nor any agency thereof, nor any of their employees, makes any warranty, express or implied, or assumes any legal liability or responsibility for the accuracy, completeness, or usefulness of any information, apparatus, product, or process disclosed, or represents that its use would not infringe privately owned rights. Reference herein to any specific commercial product, process, or service by trade name, trademark, manufacturer, or otherwise, does not necessarily constitute or imply its endorsement, recommendation, or favoring by the State of Washington or any agency thereof. The views and opinions of authors expressed herein do not necessarily state or reflect those of the State of Washington or any agency thereof.

## INDEMNIFICATION

Research supported by the U.S. Geological Survey, National Cooperative Geologic Mapping Program, under USGS award number G20AC00247. The views and conclusions contained in this document are those of the authors and should not be interpreted as necessarily representing the official policies, either expressed or implied, of the U.S. Government.

## WASHINGTON STATE DEPARTMENT OF NATURAL RESOURCES

Hilary S. Franz—*Commissioner of Public Lands*

## WASHINGTON GEOLOGICAL SURVEY

Casey R. Hanell—*State Geologist*

Jessica L. Czajkowski—*Assistant State Geologist*

Ana Shafer—*Assistant State Geologist*

### Washington State Department of Natural Resources Washington Geological Survey

#### Mailing Address:

1111 Washington St. SE

MS 47007

Olympia, WA 98504-7007

#### Street Address:

Natural Resources Bldg, Rm 148

1111 Washington St SE

Olympia, WA 98504

Phone: 360-902-1450

Fax: 360-902-1785

Email: [geology@dnr.wa.gov](mailto:geology@dnr.wa.gov)

Website: <http://www.dnr.wa.gov/geology>

#### Publications and Maps:

[www.dnr.wa.gov/programs-and-services/geology/](http://www.dnr.wa.gov/programs-and-services/geology/publications-and-data/publications-and-maps)

[publications-and-data/publications-and-maps](http://www.dnr.wa.gov/programs-and-services/geology/publications-and-data/publications-and-maps)



#### Washington Geology Library Searchable Catalog:

[www.dnr.wa.gov/programs-and-services/geology/](http://www.dnr.wa.gov/programs-and-services/geology/washington-geology-library)

[washington-geology-library](http://www.dnr.wa.gov/programs-and-services/geology/washington-geology-library)

**Suggested Citation:** Polenz, Michael; Hladky, F. R.; Anderson, M. L.; Alexander, K. A.; Tepper, J. H.; Miggins, D. P.; Legoretta Paulin, Gabriel, 2023, Geologic map of the McKenna and northern half of the Lake Lawrence 7.5-minute quadrangles, Thurston and Pierce Counties, Washington: Washington Geological Survey Map Series 2022-06, revised March 2023, originally published December 2022, 1 sheet, scale 1:24,000, 35 p. text. [[https://www.dnr.wa.gov/publications/ger\\_ms2022-06\\_geol\\_map\\_mckenna\\_northern\\_lake\\_lawrence\\_24k.zip](https://www.dnr.wa.gov/publications/ger_ms2022-06_geol_map_mckenna_northern_lake_lawrence_24k.zip)]

**Revision description:** The following mistakes related to ages reported in the original pamphlet and Map Sheet have been corrected. Corrections were made March 3, 2023.

- The abstract on both the plate and pamphlet mistakenly described an age range of "42 ± 9 ka to 187 ± 29 ka" which should have read "26 ± 5 ka to 187 ± 59 ka."
- On the Map Sheet, the description for unit Qpc included an incorrect reference to "∼1 Ma" that should have read "∼187 ± 59 ka."
- In Table 2, the age of sample GD1 was incorrectly reported as 187 ± 29.3 ka when it should have read 142.6 ± 38.2 ka.
- In Table 2, the age of sample GD2 was incorrectly reported as 142.6 ± 38.2 ka when it should have read 187.0 ± 58.6 ka.
- In Table A1, the age of sample GD1 was incorrectly reported as 26 ± 5 ka when it should have read 142.6 ± 38.2 ka.
- In Table A1, the age of sample GD2 was incorrectly reported as 26 ± 5 ka when it should have read 187.0 ± 58.6 ka.
- For samples GD8–GD16 in Table C1, the headers for the ages incorrectly showed ka when the ages were actually in Ma.



POLENZ, MICHAEL

*Michael Polenz*  
December 2022



# Contents

Introduction .....	1
Geologic Overview .....	1
Bedrock .....	1
Unlithified Deposits .....	2
Overview of Regional Structure .....	2
Methods .....	3
Geologic Mapping .....	3
Geophysics .....	3
Description of Map Units .....	3
Holocene to Pleistocene Nonglacial Deposits .....	3
Late Pleistocene Glacial and Nonglacial Sediments .....	6
Late to Middle Eocene Northcraft Formation Volcanic Rocks .....	10
Discussion .....	12
Eocene Bedrock .....	12
Quaternary Sediment .....	13
Whole Rock Geochemistry .....	16
Geophysics and Structures .....	16
Suggestions for Further Study .....	18
Acknowledgments .....	18
Worker Contributions .....	18
References .....	18
Appendix A. New Luminescence Age Estimates .....	23
Appendix B. New Detrital U/Pb Age Estimate .....	25
Appendix C. New <sup>40</sup> Ar/ <sup>39</sup> Ar Age Estimates .....	27
Appendix D. Gravity and Magnetic Data .....	33

## FIGURES

<b>Figure 1.</b> Images depicting a variety of lahar deposits found in the map area .....	5
<b>Figure 2.</b> Images showing locations of samples collected for geochemistry and dating .....	9
<b>Figure 3.</b> Total alkalis versus silica plot .....	14
<b>Figure 4.</b> Alkali-Iron-Magnesium ternary plot (AFM diagram) .....	15
<b>Figure 5.</b> MORB-normalized element abundance spider diagram .....	15

## TABLES

<b>Table 1.</b> Lithologic assemblages typical of northern-sourced and Cascade Range-sourced sediment in the map area .....	4
<b>Table 2.</b> Summary of age analyses .....	11
<b>Table A1.</b> Optically Stimulated Luminescence (OSL) and Infrared Stimulated Luminescence results from age site GD3 .....	24
<b>Table B1.</b> Detrital zircon maximum constraining ages from age sites GD3 and GD4 .....	26
<b>Table C1.</b> Summary of new <sup>40</sup> Ar/ <sup>39</sup> Ar ages from the McKenna and Lake Lawrence 7.5-minute quadrangles .....	28

## MAP SHEET

Geologic map of the McKenna and northern half of the Lake Lawrence  
7.5-minute quadrangles, Thurston and Pierce Counties, Washington

**Figure M1.** Geophysical interpretation for the map area



---

# Geologic Map of the McKenna and Northern Half of the Lake Lawrence 7.5-minute Quadrangles, Thurston and Pierce Counties, Washington

by Michael Polenz<sup>1</sup>, Frank R. Hladky<sup>1</sup>, Megan L. Anderson<sup>1</sup>, Katherine A. Alexander<sup>1</sup>, Jeffrey H. Tepper<sup>2</sup>, Daniel P. Miggins<sup>3</sup>, Gabriel Legoretta Paulín<sup>4</sup>

<sup>1</sup> Washington  
Geological Survey  
MS 47007  
Olympia, WA  
98504-7007

<sup>2</sup> Department of Geology  
University of  
Puget Sound  
1500 N Warner St. #1048  
Tacoma, WA  
98416-1048

<sup>3</sup> Argon Geochronology  
Laboratory,  
Oregon State University,  
Corvallis, OR  
97331

<sup>4</sup> Instituto de Geografía,  
Universidad Nacional  
Autónoma de México  
Ciudad Universitaria  
Del Coyoacán  
cp 04510, México, D.F.

## ABSTRACT

The map area covers the McKenna quadrangle and the northern half of the Lake Lawrence quadrangle in Washington's southern Puget Lowland. Thirty-one geochemical analyses characterize Eocene volcanic and volcanoclastic rocks of Northcraft Formation bedrock and clasts in Quaternary assemblages of volcanoclastic rocks. These Quaternary assemblages were deposited in the map area by lahars from the Cascade Range (originating from Mount Rainier and (or) nearby sources such as the Tatoosh Range). Rock types are mostly andesitic but range from basalt to rhyolite. Rocks of the Northcraft Formation are bi-modal in the map area. The Northcraft Formation includes complexly stratified, coarse, bouldery lahar deposits that are kilometers wide and hundreds of meters thick. Seven new radiometric ages from the Northcraft Formation range from about 37 Ma up to about 43.5 Ma. Preliminary analysis of aeromagnetic and gravity potential fields data is consistent with Polenz and others' (2021) idea that the Olympia geophysical lineament has northeast-down offset along segmented and bifurcated normal faults with a strike-slip component.

A thin veneer of Vashon glacial deposits as well as thicker, underlying Cascade Range-derived sediment provide productive but easily polluted aquifers for water wells. Abundant, Cascade Range-derived lahar deposits along the Nisqually River valley record life-threatening volcanic hazards. Several new age estimates from pre-Vashon sediment along the Nisqually River valley and age estimates from Polenz and others' (2021) work on similar sediment farther downstream suggest sediment ages from 26 ±5 ka to 187 ±59 ka.

## INTRODUCTION

The map area is located east of Olympia and straddles the Puget Lowland and the western foothills of the Cascade Range. Within the map area, land is primarily used for urban and rural residences, forestry, agriculture, conservation, industrial operations, and military training at Joint Base Lewis–McChord (JBLM). Quarries in both quadrangles yield aggregate from glacial outwash, and quarries in the Lake Lawrence quadrangle additionally yield volcanic bedrock.

This mapping project provides geologic context for private and public land-use decisions and for understanding geologic hazards (earthquakes, landslides, lahars, and floods) and resources (water and quarry rock) in the area. The map builds off of prior mapping in and near the study area that began in the 20th century (Bretz, 1913; Mundorff and others, 1955; Snavely and others, 1958; Noble and Wallace, 1966; Walters and Kimmel, 1968; Schasse, 1987; Walsh and others, 1987, 2003; Drost and others, 1999; Polenz and others, 2021). The map and this report offer an updated perspective on the gravity and magnetic lineament

known as the 'Olympia structure'—first noted by Daneš and others (1965)—and recently interpreted as a fault (for example, Polenz and others, 2021). The map and report also provide insight into rock types, properties, ages, and the processes that formed the landscape in the map area—from Eocene volcanism that formed the upland hills, to Pleistocene glacial scour, deposition, and post-glacial alluviation and lahar deposition.

## GEOLOGIC OVERVIEW

### Bedrock

Southern uplands in the map area expose rocks of the middle- to late- Eocene Northcraft Formation, which consist of stratovolcanic, subaerially erupted, mostly andesitic flows and volcanoclastic rocks (Snavely and others, 1951, 1958; Buckovic, 1979; Hagen, 1987; Schasse, 1987; Walsh and others, 1987; Phillips and others, 1989). These rocks are associated with the ancestral western Cascade volcanic arc of southwestern Washington and western

Oregon (McBirney, 1978; Stanley and others, 1989). The arc is deeply eroded, broader than the modern Cascade arc, and centered farther west. Although rock ages observed west of and within the map area (Polenz and others, 2021; this study) suggest a slight eastward-younging trend within the arc, the more regional structural pattern and geographic distribution of rock ages within the southwest Washington portion of the arc (Walsh and others, 1987; Phillips and others, 1989) remain poorly understood. Any trend within the Washington portion of the arc appears less systematic and more complex than that in Oregon, where several studies suggest a mostly east-dipping sequence of commonly eastward-younging Pliocene and older overlapping shield and stratovolcanoes and their flanking deposits (Peck and others, 1964; Fiebelkorn and others, 1982; Wiley and Hladky, 1991; Hladky, 1992, 1998; Hladky and McCaslin, 2006; Madin and others, 2006).

Geophysical models (Finn, 1990; unpublished records, Washington Geological Survey (WGS)) indicate that aside from the Northcraft Formation, rocks in the subsurface of the map area include the early Eocene Crescent Formation basalt of the Siletzia terrane (Wells and others, 2014; Eddy and others, 2016, 2017) and ultramafic, relict mantle rocks deeper in the subsurface.

## Unlithified Deposits

Glacial till and outwash cover most of the map area with sediment derived from the Cascade Range, the San Juan Islands, and the Coast Mountains of British Columbia. Most of this lithologically diverse drift was moved into the map area by Cordilleran glacial ice and meltwater during the late Wisconsinan Vashon stage of the Fraser Glaciation (marine oxygen isotope<sup>1</sup> stage 2, MIS 2), when ice reached its southern terminus in the map area (Bretz, 1911, 1913; Noble and Wallace, 1966). Radiocarbon dates suggest that the ice advanced gradually but collapsed quickly (Polenz and others, 2015). Polenz and others (2015) estimated that the Vashon glacial advance and retreat occurred between about 15.3 and 16 ka, revising Porter and Swanson's (1998) earlier assessment of 16.75 to 16.95 ka. An ancestral Nisqually River additionally moved gravelly alluvium westward from the Cascade Range into the map area, with sediment pulses likely responding to both volcanic activity and Pleistocene glaciations of Mount Rainier and surrounding areas (Crandell and Miller, 1974; Walsh and others, 2003).

Glacial scour and deposition from ice and meltwater led to a patchwork of geomorphic features and associated sediment that remain readily apparent in lidar images: drumlins and flutes record southwestward ice movement (Brown and others, 1987), kettles and eskers mark where stagnant ice wasted away

(Haugerud, 2009; Polenz and others, 2009), and outwash channels and terraces document meltwater pathways (Logan and others, 2009) and post-glacial Nisqually River incision. In addition, enigmatic Mima mounds (Bretz, 1913; Washburn, 1988; Logan and Walsh, 2009; Horwath Burnham and Johnson, 2012; Gabet and others, 2016) are present on some gravelly glacial outwash surfaces.

## Overview of Regional Structure

Throughout western Washington, northwest-trending bands of seismicity within the Cascade Range trend toward basin-bounding, northwest-striking, dextral oblique faults and east- or west-striking reverse faults in the Puget Lowland (Gower and others, 1985; Brocher and others, 2001). These faults collectively accommodate ongoing crustal shortening and plate rotation in the Cascadia forearc (Wells and McCaffrey, 2013; McCaffrey and others, 2013; Wells and others, 2014). In the map area, the northwest-oriented Olympia structure marks the southwestern edge of the Tacoma basin, and the Olympia structure's orientation and northeast-down offset seem to fit the above-mentioned framework of faults, yet understanding of the Olympia structure and what hazards it may present has remained elusive (Sherrod, 2001; Magsino and others, 2003; Walsh and Logan, 2005; Odum and others, 2016; Polenz and others, 2016, 2021).

The Olympia structure corresponds to a northeast-down gravity gradient first noted by Daneš and others (1965). It extends from the Olympic Mountains to the map area and coincides with a distinct aeromagnetic lineament. Northeast of the Olympia structure, the basin deepens northward to an estimated depth of 5–7 km (Pratt and others, 1997; Brocher and others, 2001; Van Wagoner and others, 2002); the north side of the Tacoma basin is flanked by the active Tacoma fault (Brocher and others, 2001; Nelson and others, 2008). Along the part of the Olympia structure northwest of the map area, studies have identified: (1) post-glacial faulting on the northeast side of the geophysical lineament (Clement and others, 2010; Odum and others, 2016), (2) heavily disturbed Quaternary sediment on the southwest side (Polenz and others, 2016), and (3) evidence for Holocene subsidence in the southern Puget Lowland (Sherrod, 2001). A lack of bedrock exposures between the Olympia structure and the Cascade Range farther east seems consistent with an actively deepening Tacoma basin. Yet compared to structures farther north in western Washington, recorded seismicity is minimal along and south of the Olympia structure. No Quaternary tectonic deformation has to date been clearly connected to the Olympia structure itself, and the subsurface geometry and kinematics of the Olympia structure remain poorly defined. In the adjacent Vail and Tenalquot Prairie quadrangles west of the map area, Polenz and others (2021) concluded that the Olympia structure is a fault—probably a normal fault with multiple strands, based on geophysical interpretations, and hereinafter we refer to the structure as the Olympia fault. At the southern margin of Polenz and others' (2021) map area, Snavely and others (1958) showed three northwest-striking normal faults parallel to the Olympia fault. The normal offset on all four northwest-striking faults implies northeast–southwest extension. Polenz and others (2021) also suggested that the shallow subsurface of the Tacoma basin near the Olympia fault holds >2,500 m of strongly magnetic

<sup>1</sup>MIS: global marine oxygen isotope stage curve, where even-numbered stages are used as a proxy for timing and intensity of global glacial periods (Morrison, 1991; Lisiecki and Raymo, 2005). For discussion of Cordilleran ice advances into the Puget Lowland, see Booth and others (2004), Troost and Booth (2008), Polenz and others (2013, 2015), and Troost (2016). For timing of the MIS 2 ice advance into the map area at the southern limit of the Vashon glaciation, we refer to Polenz and others' (2015) fig. 3 and discussion, although the southern tip of their fig. 3 should have been extended south beyond the Deschutes River.



volcanic and volcanoclastic deposits, and fault-parallel intrusions, probably of the Eocene Northcraft Formation, suggesting that northeast-down offset along the Olympia fault could be entirely Eocene. Yet no more than 12.6 km southwest of the map area, faults of a similar orientation appear to be transpressional (Snively and others, 1958; Polenz and others, 2018, 2019, 2020; Sadowski and others, 2018, 2019). This suggests that northeast extension may be only part of the deformation along the Olympia fault, or that the Olympia fault responded to a different stress field (perhaps at a different time) than the faults farther southwest.

## METHODS

### Geologic Mapping

We identified units from field observations in the McKenna quadrangle and northern half of the Lake Lawrence quadrangle in the summer and fall of 2021. We collected field data and constructed preliminary field-based maps using Esri's ArcMap. We refined the field mapping through geochemical analyses; petrographic review of thin sections; luminescence,  $^{40}\text{Ar}/^{39}\text{Ar}$ , and U/Pb age analyses; clast counts; geophysical data; analysis of well and boring records; consideration of geotechnical reports and prior geologic mapping and studies; aerial orthophotos; and geomorphic features identified from lidar. We used a lidar-based digital elevation model (DEM) with a 2-m grid resolution (Pierce County, 2011; Thurston County Geodata Center, 2011; U.S. Geological Survey, 2016; JBLM written commun., 2021) to estimate site elevations and derive hillshade images, contours, and other products. We identify some locations along the Nisqually River by river miles (RM) downstream of the Alderwood dam, such that RM17.48 marks the eastern (upstream) map edge. An 'L' or 'R' following a river mile number indicates whether a site is located left (L) or right (R) of the river when looking downstream; R therefore is in Pierce County while L is in Thurston County. We otherwise report measurements and data using the metric system; the one exception is elevation, which we report in feet-above-mean-sea-level (ft) to aid in comparison with topographic maps. Edge mismatches with the adjacent Tenalquot Prairie and Vail quadrangles (Polenz and others, 2021) are intentional based on insights from our latest mapping. We used the geologic time scale of the United States Geological Survey (USGS) Geologic Names Committee (2018). Where that scale lacks Epoch subdivisions, we referred to Walker and Geissman (2009).

### Geophysics

We collected 191 new gravity measurements to construct a refined gravity map with particularly dense station spacing across selected areas of interest, mainly the Olympia fault. In addition, we applied a quantitative algorithm to this map to select high-amplitude linear gradients (or "max-spots"; Appendix D; Fig. M1A). Aeromagnetic data (Fig. M1) are compiled from Blakely and others (1999, 2020). We also applied the max-spot algorithm in our interpretation of aeromagnetic gradients ("lineaments", Fig. M1A). Forward-modeled isostatic gravity and aeromagnetic profiles along line X-X' (Fig. M1B) quantitatively test subsurface interpretations developed from map-view geologic

and geophysical data. Rock density and magnetic susceptibility measurements of samples from 63 outcrops within and beyond the map area helped constrain these models (unpublished records, WGS; Appendix D). These geophysical data and analyses supplemented our geologic interpretations and are in the Data Supplement. Appendix D contains details of gravity, magnetic, rock property, and modeling methods.

## DESCRIPTION OF MAP UNITS

### Holocene to Pleistocene Nonglacial Deposits

- |         |  |
|---------|--|
| af      | <b>Artificial fill (Holocene)</b> —Cobbles, pebbles, sand, silt, clay, and boulders, all in various amounts, engineered and non-engineered; placed to raise roadbeds and other surfaces. Excludes small or shallow fills (less than 1.5 m thick) such as most road-related deposits.   |
| ml      | <b>Modified land (Holocene)</b> —Locally derived soil, cobbles, pebbles, sand, silt, clay, and boulders, all in various amounts, reworked by excavation and (or) redistribution that modified topography; includes gravel pits and other developments. Excludes small or shallow reworking such as most residential site preparation and road-related modifications with excavations or deposits less than 1.5 m deep or thick.  |
| Qp      | <b>Peat (Holocene to late Pleistocene)</b> —Organic and organic matter-rich sediment (peat, gyttja, muck, silt, clay, and sand) in flat-bottomed depressions or other poorly drained flat areas; mostly mapped where lidar reveals landforms that suggest absence of appreciable, active alluvial sedimentation and where we interpret true-color or infrared aerial photos as suggesting hydrophilic vegetation and (or) wet conditions. Unit Qp is post-glacial in age.  |
| Qa, Qoa | <b>Alluvium (Holocene to late Pleistocene)</b> —Floodplain and channel sediment of mostly andesitic pebbles, cobbles, boulders, sand, silt, clay, and peat, all in various amounts; gray to pale gray and brown to pale brown, weathers brown, orange, red, and yellow; fresh to mildly weathered, though some exposures include more weathered particles that were proximally reworked from older, more weathered deposits; loose; mostly well rounded and moderately to well sorted; cross-bedded or channel trough bedded where gravelly, and planar-bedded in sandy and silty flood plain deposits; mostly reworked from unit Qpc, and lithologically similar to that andesite-rich older alluvium, but in some exposures reworked from Vashon Drift or some mix of the two sources. In the Nisqually River valley, unit Qa locally includes Mount Rainier-derived debris flow diamicton, mud flow deposits, and lahar run-out deposits. Where those are well-exposed and extensive, they are separately mapped as unit Qvl. Alluvial fan deposits are locally included in unit Qa where separate mapping proved impractical due to map scale. The |

**Table 1.** Lithologic assemblages typical of northern-sourced and Cascade Range-sourced sediment in the map area.

Northern-sourced	Cascade Range-sourced
Mostly Cascade Range-sourced (see column on right). But: Includes varied amounts (commonly only trace quantities) of schist, gneiss, bright pink garnets, epidote, and granitic rocks that contain orthoclase. Lithologically diverse and rich in polycrystalline quartz (Walsh and Logan, 2005). <60% intermediate to felsic volcanic rocks. >15% mafic igneous rocks (basalt and gabbro).	>60% intermediate to felsic volcanic rocks, mostly porphyritic andesite; less abundant dacite, felsic to intermediate rocks, and basalt. Other rock types absent or rare. Usually less basalt, sedimentary rocks, and according to Noble and Wallace (1966), less granodiorite than in northern-sourced drift. Less lithological diversity and less polycrystalline quartz than in northern-sourced assemblages of Walsh and Logan (2005). Large quantities of hypersthene in rocks from Mount Rainier (Noble and Wallace, 1966). A faintly lavender hue in gray sand exposures.

fan deposits tend to be more angular, less sorted, and less consistently bedded than other deposits in units Qa and Qoa. Unit Qa forms a highly permeable and productive, generally unconfined aquifer. These traits render the aquifer sensitive to pollution and the surface locally prone to dry soil. Unit Qa is mapped where alluvial transport appears active. The unit is postglacial in age but may locally include alluvium of pre-Vashon age south of the ice limit near the southwestern map corner.

Unit Qoa identifies alluvium that is no longer moving or accumulating. Unit Qoa includes a few relict alluvial fans, which, unlike active fans, are not subject to increased debris flow hazards. Four relict fans would be large enough to map separately but are included in unit Qoa to avoid map clutter. These fans are located as follows: near the western map edge 450 m south of the Nisqually River, southeast of the Nisqually River 150 m upstream of RM29, at the southern map edge west of the Deschutes River, and along Hull Creek 1.5 km north of the southern map edge. Unit Qoa is post-glacial in age.

**Qaf Alluvial fan (Holocene to late Pleistocene)**—Diamicton, pebbles, sand, silt, cobbles, and boulders, all in various amounts, deposited in broad fans where debris flows and floods spill from confined channels onto broader, less steeply sloping surfaces; gray to brown; loose; subangular to rounded; moderately to poorly sorted; mostly poorly bedded, but ranging to unbedded and well bedded; sourced from upslope deposits and therefore lithologically similar to those; 1.5–6 m thick in most exposures, but may exceed 10 or 12 m thickness northeast of Jonas Hill (NE¼ of the NW¼, Sec. 31, T16N R2E) and 0.8 km southeast of Reichel Lake (N½ of the NE¼, Sec. 5, T15N R2E). Unit Qaf was mostly mapped from fan-shaped landforms expressed in lidar and is mostly deposited by hazardous debris flows and floods. Unit Qaf is postglacial in age except possibly for one location that may include deposits of pre-Vashon age south of the ice limit near the southwestern map corner.

**Qls Landslide deposits (Holocene to Pleistocene)**—Sand, silt, clay, pebbles, cobbles, and boulders, all

in various amounts, derived from deposits upslope; weathering is varied; particles angular to rounded; mostly loose, unsorted, and jumbled, but stratified in some exposures and internally stratified and (or) compact in some landslide blocks; mostly mapped from landforms expressed in lidar (for example, hummocky slopes, deranged and disrupted drainages, disrupted or irregular slopes, tilted benches in hillsides, and concave upper and convex lower slope forms). Similar landforms are locally common—but not necessarily indicative of landslides—among Northcraft Formation volcanic rocks and in glacial deposits; we may therefore have erroneously mapped some landslides and failed to map others. Abundant landslides in the hills of the Lake Lawrence quadrangle suggest that unit Evc<sub>n</sub> is particularly landslide-prone and is the main source of common and conspicuous landslide blocks measuring several meters in diameter. Landslides in unlithified sediment along active cutbanks of the Nisqually River are also common, but none are mapped because their deposits are quickly removed by the river. Unit Qls is generally post-glacial in age, but landslides south of the ice limit and some larger, deep-seated landslides in bedrock may be of pre-Vashon age.

**Qmw Colluvium (Holocene to Pleistocene)**—Loose soil, rocks, sand, silt, and clay, all in various amounts, deposited by shallow ravel and soil creep; locally includes small landslides and alluvial fans, but fan-shaped deposits in unit Qmw are typically steeper than those in unit Qaf, and based on lidar, tend to have less well-defined upslope feeder channels; shown where colluvium masks the underlying geology; mostly identified from landforms, and may locally include exposures of underlying deposits, especially where those are volcanic; not mapped where creeping, clayey soils appear to mantle otherwise undisturbed, smooth slope surfaces (that we mapped as underlying units). Unit Qmw is post-glacial in age except possibly south of the ice limit, where it may locally be pre-Vashon in age.

**Qvl Lahar deposits and lahar run-out deposits (Holocene to late Pleistocene)**—Diamicton and gravel of all sizes,



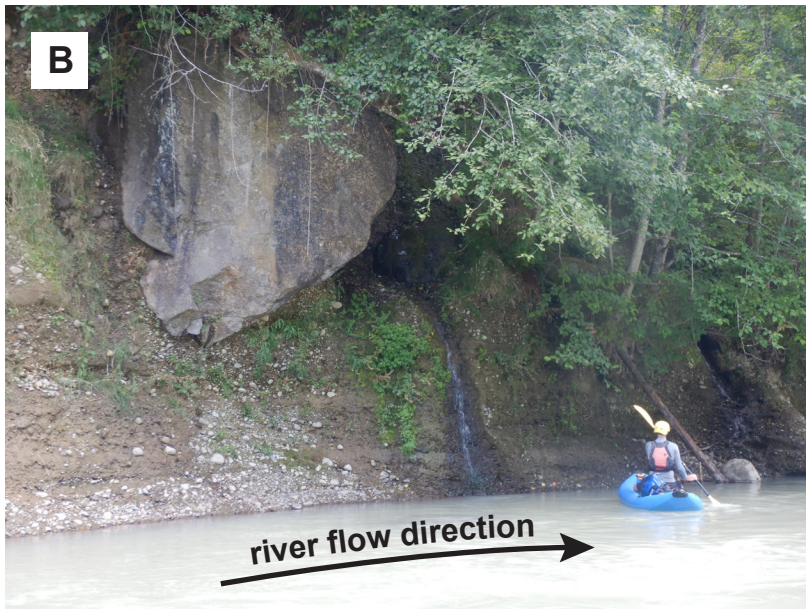


**Figure 1.** Images depicting a variety of lahar deposits found in the map area. See also additional images in Figs. 2A and C. Whereas all these lahar deposits are Quaternary, an Eocene lahar deposit within unit Evc<sub>n</sub> is pictured in the foreground of the pamphlet cover photo. **A.** Lahar deposit with mostly angular andesite (to dacite), commonly pumiceous clasts and unsorted matrix rich in volcanic glass shards and small ash fragments. **B.** Lahar deposit at Nisqually RM25.09L, with scattered, faceted boulders in unbedded pre-Vashon gravel. **C.** Debris flow at Nisqually RM26.29L—not necessarily a lahar. The deposit consists of boulders (some faceted) in unbedded pre-Vashon gravel, mapped as unit Qv1?. This debris flow exposure is unique among all those we observed in that it contains boulders of till and sandstone. Age is Quaternary but unresolved relative to Vashon ice incursion. Mild induration may be from lahar deposition or glacial overriding. Underlying pebble gravel appears to be pre-Vashon (unit Qpc), based on compaction and weathering. Overlying alluvium appears to be post-glacial Nisqually River sediment (unit Qoa). The pictured site, near the northern end of the map area, is the only debris flow exposure in which we identified northern-sourced till fragments and sandstone. All other observed debris flow deposits were full of andesite, pumice, and less commonly dacite, diorite or gabbro—rock types consistent with Cascade Mountain sources at or near Mt. Rainier.



sand, prominent boulders up to >3 m diameter (Fig. 1); clasts mostly andesite, followed by other Cascade Range-sourced rocks (see Table 1 and *Late Pleistocene Glacial and Nonglacial Sediment*); matrix mostly sand; medium gray to variegated (mostly dark to pale gray, lavender, lilac, red, and greenish gray); mildly to moderately weathered; generally loose but commonly somewhat stiff and crusty; clasts mostly rounded to well-rounded but ranging to angular; unsorted in diamicton, unsorted to poorly sorted in gravel, poorly to moderately sorted in sand; unbedded, less commonly poorly bedded, and, in exposures that we interpret as hyperconcentrated flow deposits, marked by swirl patterns and locally oversteepened bedding; matrix rich in lapilli, pumice, and glass fragments; observed unit thickness 1.5–6 m; intermittently exposed along banks of the Nisqually River (Fig. 1B) and on terraces upslope thereof.

We interpret unit Qv1 as deposits from lahars (diamicton), lahar run-outs (diamicton, gravel, sand), and hyperconcentrated flows (mostly sand, commonly pumiceous, some gravel). Boulders scattered in some channel reaches of the Nisqually River appear to mostly be lag deposits of units Qv1 and Qpvl where the river eroded lahar deposits. Pat Pringle and Norman McLeod (written and oral communications, 2021) attribute pumiceous sand on some Holocene terraces, for instance near well site W8 (RM22.55R), to the National Lahar (>800 and <1,820 ± 300 14C yrs. BP; Scott and others, 1995). Unit Qv1 commonly rests on sharp, conformable to unconformable and locally erosional contacts with underlying sediment. We observed no contacts with upsection sediment (usually units Qa or Qoa). Clast composition and geography suggest provenance from Mount Rainier and vicinity—except at RM26.29L (Fig. 1C), where boulders of sandstone, mudflow diamicton, and till fragments with northern-sourced granite suggest either a lahar that bulked up on northern-sourced drift or a periglacial debris flow that need not have started as a lahar—such as the Tanwax Ohop Valley flood (Pringle and Goldstein, 2002; Parker and others, 2008). Unit Qv1 is mapped where lahars and lahar run-out deposits are post-glacial or their stratigraphic position relative to Vashon Drift is unresolved.

## Late Pleistocene Glacial and Nonglacial Sediments

### VASHON DRIFT

**Qgo** **Recessional or proglacial outwash, undivided (late Pleistocene)**—Pebble gravel, less commonly cobble and boulder gravel, pebbly sand or sand; northern-sourced (Table 1); gray to pale gray, or mildly weathered to pale brown, brown, or variegated with iron stains; loose and commonly cohesionless; well rounded to subrounded; moderately sorted to well sorted and in gravel facies clast supported, locally with matrix and interbeds of silt and sand; otherwise unbedded. Terrace

risers suggest that unit thicknesses of 1.5–10 m are common and that subunits Qgog and Qgoj may exceed thicknesses of 18 m where Lackamas Creek approaches the eastern map edge. Unit Qgo tends to form flat to gently sloping terraces (or terrace flights) with relict, mostly braided channel forms. Undivided unit Qgo is mapped where observations or map scale did not permit mapping of its textural or paleoenvironmental subunits. Unit Qgo is of Vashon recessional age and stratigraphically overlies Vashon Till (including end moraines) and most ice-contact deposits.

Some outwash near the ice margin includes deposits from high-discharge events (Pringle and Goldstein, 2002; Polenz and others, 2021). Pringle and Goldstein (written commun., 2018) strongly support Parker and others' (2008) assertion that an andesite-rich, Mount Rainier-sourced flood (the “Tanwax flood”) flowed across the map area (Pringle and Goldstein, 2002), and deposited diamicton west of Tenino (figs. 5 and 6 of Polenz and others, 2018). We did not definitively identify debris flow or flood runout deposits within unit Qgo, but the Tanwax flood pathway would suggest that both are present. A debris flow deposit tentatively mapped as unit Qv1? at RM26.29L (Fig. 1C) may instead be such a flood deposit and is in a possible Tanwax flood pathway suggested by Pringle and Goldstein (2002). Unlike all other observed lahar deposits, this exposure includes northern-sourced boulders and till fragments, but we question if it is from the Tanwax flood because its elevation at <240 ft is far below the >400 ft elevation of ice-marginally west-directed outwash surfaces that the Tanwax flood passed at the western map edge. Locally subdivided into:

**Qgog** **Recessional or proglacial outwash gravel (late Pleistocene)**—Loose pebbles, cobbles, and boulders, in various amounts, commonly with sandy matrix and sand lenses or interbeds; debris flow deposits (diamicton) not definitively observed but suggested in the map area based on high discharge events such as the Tanwax flood, and possibly mismapped as unit Qv1? at RM26.29L (see also Fig. 1C undivided unit Qgo); northern-sourced (Table 1); tan to gray; variably sorted; mostly well rounded. Unit thickness is mostly unconstrained, but terrace risers suggest that unit thicknesses of 1.5–10 m are common and unit thickness may exceed 20 m and 18 m at the western map edge southwest of Jonas Hill and where Lackamas Creek approaches the eastern map edge. Clusters of mima mounds are revealed by lidar images, for instance southeast of Four Corners (donation land claim Sec. 37, T17N R2E). Although their development remains enigmatic (see *Geologic Overview*), we associate Mima mounds with unit Qgog because they appear



to be restricted to Vashon outwash gravel surfaces.

**Qgos**     **Recessional or proglacial outwash sand (late Pleistocene)**—Sand and silt, locally pebbly, cobbly, or containing interbeds of gravel; northern-sourced (Table 1); gray to brown; loose; clasts moderately to well rounded; generally well sorted; unbedded to planar bedded; sand and silt composition rich in polycrystalline quartz. Qgos unit thickness is mostly unconstrained, but we observed 2.5 m minimum thickness in a small pit near the northwestern map corner (Sec. 1, T17N R1E), and well log W38 suggests 8 m thickness just south of the border between the Lake Lawrence and McKenna quadrangles, about 2.3 km east of the western map edge.

**Qgoi**     **Recessional ice-contact outwash, undivided (late Pleistocene)**—Northern-sourced sand and gravel (Table 1) deposited in ice-contact braid plains or channels; also sand or mixed sand and gravel in kettle walls, and sand or silt in kettle bottoms, some of which are draped with post-glacial peat where kettle bottoms are flat; tan to gray; loose; moderately to well-rounded and sorted; unbedded to planar or gently cross-bedded in lake settings, and gently cross-bedded in channels or braid plains, but commonly with bedding locally oversteepened and (or) chaotic and disrupted by kettle collapse. Qgoi unit thickness is mostly unconstrained, but we probably observed 10 m in a Nisqually River cutbank at RM23.6R, and kettle depths, swales, and terrace risers suggest minimum unit thicknesses of 27 m south of the Deschutes River (Secs. 28-30, 32, and 33, T16N R2E), 18 m where Lackamas Creek approaches the eastern map edge, 17 m southeast of Reichel Lake, 15 m at a site 2.3 km east of the northwestern map corner, and 12 m in the town of McKenna at a location south of SR507 and west of the Nisqually River.

**Qgosj**     **Recessional ice-contact outwash sand (late Pleistocene)**—Sand deposited in ice-contact lakes; may locally include gravel and sand deposited in kettle walls, braid plains, or channels, and sand or silt in kettle bottoms; northern-sourced (Table 1); tan to gray; loose; moderately to well-rounded and sorted; unbedded to planar

bedded, planar to gently trough cross-bedded where gravelly, but bedding locally oversteepened and (or) chaotic and disrupted by kettle collapse. Qgosj unit thickness is mostly unconstrained, but terrace risers and kettles suggest that unit thickness may exceed 30 m west of Nelda Lake.

**Qgim**     **End moraine (late Pleistocene)**—Pebbly to cobbly till, pebbles, sand, cobbles, silt, clay, and boulders, all in various amounts; northern-sourced (Table 1); gray, tan, and reddish brown; loose to compact; unbedded in till, unbedded to bedded in other facies. Topographic relief suggests that unit thickness commonly exceeds 15 m and may locally exceed 30 m. Boulders (glacial erratics) commonly rest on the surface of unit Qgim. Landforms within unit Qgim tend to be hummocky and kettled, but surfaces smoothed by meltwater, outwash, and localized lake deposits are also common. Landforms in unit Qgim commonly resemble those in landslides, but unit Qgim tends to be more permeable, with somewhat more effective drainage and commonly more organized drainage incision patterns. Compared to units Qgic and Qgt, unit Qgim generally forms more hummocky and less streamlined surfaces with little or no evidence of drumlins and flutes. Lesser compaction in most exposures additionally separates it from unit Qgt. Unit Qgim dropped out of melting, mostly stagnant ice at the southern ice margin and is locally reworked as (or supplemented by) ice-contact outwash, which locally resulted in kame terrace settings mostly south of the Deschutes River. Many exposures of unit Qgim are more weathered than is elsewhere typical of Vashon Drift. This suggests that older sediment near the ice margin was commonly reworked from nearby substrate into Vashon deposits.

**Qge**     **Esker (late Pleistocene)**—Pebbles and sand; northern-sourced (Table 1); medium gray; lightly to moderately weathered; mostly loose; clasts well rounded; well sorted; most exposures are distinctly channel trough-bedded or cross-bedded, with beds commonly oversteepened because the source water, being confined beneath ice, locally flowed uphill, or because bedding was deformed when englacial and supraglacial deposits sank to the ground during ice melt. Unit Qge was deposited by subglacial, englacial, and supraglacial meltwater and is mostly found amid, adjacent to, or resting on unit Qgic. Units Qp and Qgo locally onlap it. Unit Qge forms distinctively sinuous hills which we used to identify most of the unit. A dense cluster of unit Qge northeast of the town of McKenna locally contains small patches of other deposits in troughs, mainly units Qp and Qgic.

**Qgic** **Ice contact deposits (late Pleistocene)**—Undivided till and outwash, consisting of loose to compact diamicton, pebble gravel (locally cobbly) and sand; northern-sourced (Table 1); pale gray to brown and reddish brown; mildly weathered; mostly loose and crumbly in ablation till and outwash, ranging to compact in lodgment till, but typically lacking near surface exposures of thick, continuous, or widespread sheets of lodgment till, though small till exposures and detrital till fragments are common. Particle sizes in unit Qgic range from cobbles to medium sand, with finer particles common in till matrix and boulders locally in till and outwash. Rounding, sorting, and unit thickness are varied. Unit thickness is mostly unconstrained, but well records and exposures in road cuts and stream cuts within and outside the map area suggest that the unit is typically 1.5–10 m thick. Unit Qgic is marked by irregular landforms such as eskers (mapped as unit Qge where clearly identified and large enough to map), kettles, and rounded channels that are mostly relict and in many instances connect to eskers. These landforms document sediment deposition and meltwater scour beneath, in, or on stagnant ice. Drumlin and flute surfaces in unit Qgic are usually fainter and less regular than those in unit Qgt but still record some ice movement.

**Qgt** **Lodgment till (late Pleistocene)**—Diamicton containing boulders, smaller rocks, and sand, with an unsorted or poorly sorted matrix comprised of sand to clay-sized particles, in various amounts; northern-sourced (Table 1); matrix supported in nearly all exposures; gray to pale reddish brown; mildly to moderately weathered; mostly compact to very compact, acts as an aquitard, not usually penetrated by roots; clasts well rounded to faceted or angular, and commonly striated; matrix mostly angular; thickness in map area mostly unknown and likely to pinch out locally; thickness mostly unconstrained, with the thickest observed exposure in the map area at least 6 m thick (in the SE ¼ of the NE ¼, Sec. 4, T16N R2E); unsorted; unbedded but in some exposures flow banded (resembling bedding). Unit Qgt is deposited directly by glacial ice and usually includes a loose, surficial cover of 0.5–3 m of ablation till and (or) outwash clay, silt, sand, and gravel. That loose cover appears to be the main parent material for post-glacial soil, whereas underlying compact lodgment till tends to be mostly unweathered. Till in unit Qgt is in most exposures more compact and resists root penetration and water percolation more effectively than unit Qgic. Unit Qgt tends to be associated with distinctly elongate, northeast–southwest-oriented hills (drumlins) and troughs (flutes) that are most strongly developed in the northeastern quarter of the McKenna quadrangle. Compared to unit Qgic, unit Qgt tends to be accompanied by better-developed flutes and drumlins and fewer landforms whose preservation would signal stagnant ice (subglacial meltwater channel scour,

kettles, eskers), and we used landforms to help delineate unit boundaries between units Qgic and unit Qgt. Based on relatively few, isolated exposures mostly along Nisqually River valley walls, unit Qgt generally overlies unit Qpc. The only exception we observed is unit Qgt resting on unit Qga northeast of the Nisqually River (RM23.5R–26.5R), where unit Qga is shown as a line.

**Qga**

**Advance outwash (late Pleistocene)**—Fluvial pebble gravel and less commonly cobble gravel, boulder gravel, sand, silt, and clay; northern-sourced (Table 1); gray to light brown; compact, but commonly lacking cohesion in well-rounded, well-sorted gravel or sand intervals that resemble loose recessional outwash; mostly moderately or well rounded. Unit Qga is distinguished from recessional outwash by greater compaction from overriding ice and stratigraphic position beneath Vashon Till (unit Qgt). Unit Qga is shown on the map only by a line northeast of the Nisqually River, between RM23.5R and 26.5R. This line is queried where the presence of the unit is speculative

## PRE-VASHON SEDIMENT

**Qpc**

**Pre-Vashon alluvium from the Cascade Range, undivided (late Pleistocene)**—Pebbles, cobbles, bouldery gravel and diamicton, sand, silt, clay, and minor peat; Cascade Range sourced (see Table 1 and *Late Pleistocene Glacial and Nonglacial Sediments*); pale gray to light brown, reddish brown, and pinkish brown; generally more weathered than Vashon Drift; compact; sand usually rich in plagioclase and in andesitic, commonly glassy volcanic lithic fragments, followed by quartz and (or) K-feldspar and usually less abundant opaque minerals, pyroxene, biotite, iddingsite, and other minerals. Unit Qpc forms most sidewall exposures of the Nisqually River valley. Nearly all diamicton and bouldery deposits within unit Qpc appear to be lahar deposits (some of which are separately mapped as unit Qpvl; Fig. 1). Unit Qpc reaches at least 60 m in thickness and typically seems to immediately underlie Vashon till (units Qgt, Qgic, and Qgim) except where unit Qga is mapped along RM23.5R–26.5R. We obtained age estimates for unit Qpc in and near the map area to test Walters and Kimmel's (1968) suggestion of Miocene Mashel Formation between Nisqually RM17.5R and RM20R. At age site GD2 (RM17.1R, 420 m east of the map area and 200 m north of where cross-section A–A' meets the eastern map edge), sediment at river level suggests deposition occurred  $187.0 \pm 58.6$  ka during MIS 6, and detrital zircon ages from the collocated age site GD3 require deposition after ~1 Ma. Slightly farther upstream, clasts in a lahar deposit with polygenetic clast content 25–30 m above the river level along the eastern map edge require deposition after  $1.16 \pm 0.01$  Ma (GD8–GD10, RM16.7L). These ages are all Pleistocene and indicate that Walters and Kimmel's (1968) suggestion of Mashel



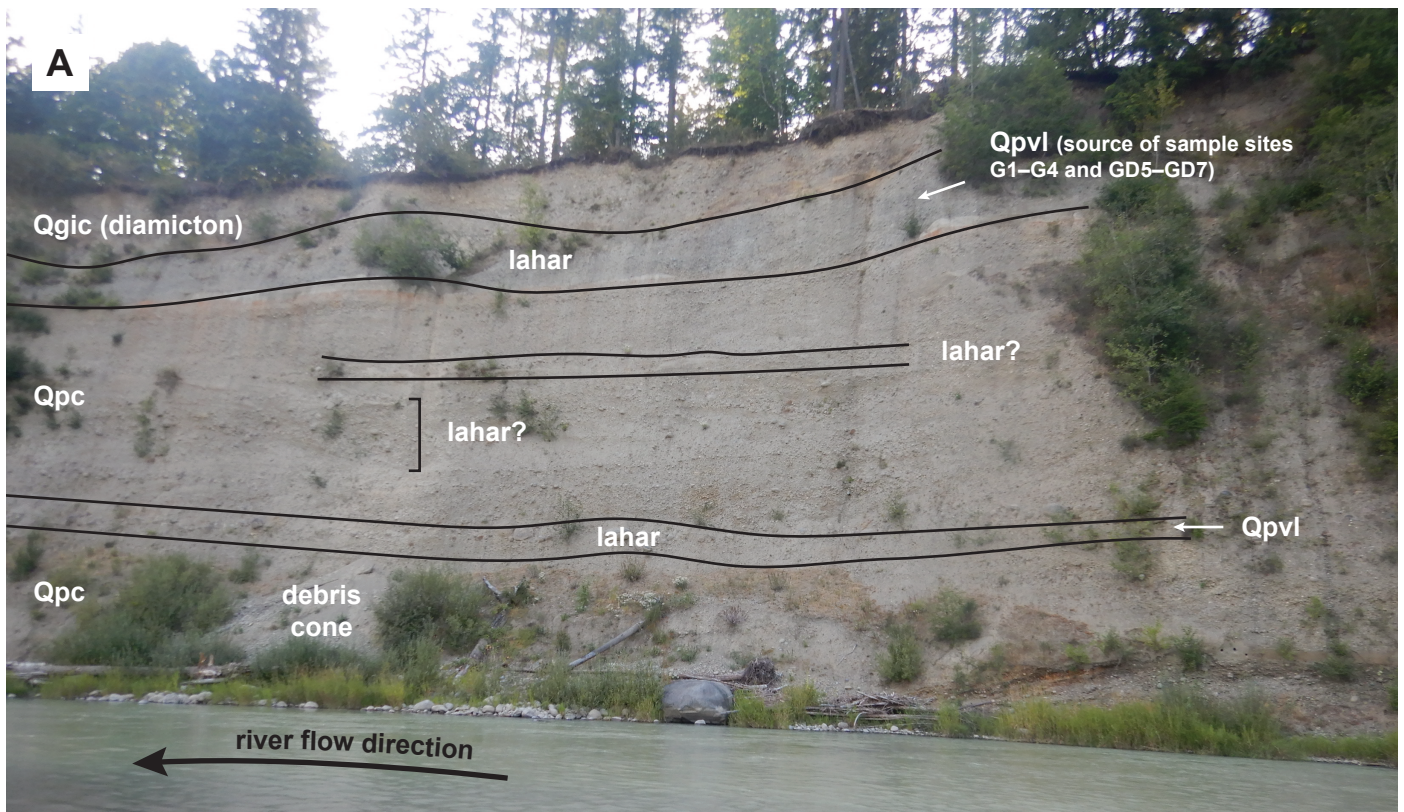


**Figure 2.** Images showing locations of samples collected for geochemistry and dating. **A.** Deposits from at least two lahars are exposed below Vashon Drift in a 44-m-high Nisqually River cutbank at JBLM. **B.** Sampling for luminescence age GD1 at base of Nisqually River cutbank. **C.** Uppermost lahar from just below Vashon Drift. Debris cone from recent rock fall provided access to lahar clasts for  $^{40}\text{Ar}/^{39}\text{Ar}$  age sites GD5–GD7.



Formation was erroneous. Farther downstream, clasts in a lahar deposit 33–38 m above the river level at JBLM (Fig. 2, RM28.3R) require deposition after  $259 \pm 14.8$  ka (GD5–GD7), and a luminescence age from the base of the same cliff suggests deposition  $142.6 \pm 38.2$  ka (GD1). A late MIS 3 age ( $26 \pm 5$  ka) is suggested for a spot 47 m above the river level that is located 1.2 km west of the map area (RM31L, age site GD3 of Polenz and others, 2021). Walsh and others (2003) suggested that deeply weathered, striated boulders downstream of that site may be lag deposits from Cascade Range-sourced Hayden Creek Drift or (older) Wingate Hill Drift.

**Qpvl** **Pre-Vashon Lahar deposits (late Pleistocene)**—Diamicton and gravel of all sizes, prominent boulders up to >3 m in diameter (Fig. 1), and sand; clasts mostly andesite, followed by other Cascade Range-sourced rocks (see Table 1 and *Late Pleistocene Glacial and Nonglacial Sediments*); matrix tuffaceous, mostly sand-sized; medium gray to variegated—mostly dark to pale gray, lavender, lilac, red, and greenish gray; mildly to strongly weathered; compact; clasts mostly rounded to well rounded but ranging to angular; unsorted in diamicton, unsorted to poorly sorted in gravel, poorly to moderately sorted in sand; unbedded, less commonly poorly bedded, and in hyperconcentrated flow deposits (observed in postglacial equivalent unit Qvl), unit is marked by locally oversteepened bedding with swirl patterns; matrix rich in lapilli, pumice, and glass fragments; observed unit thickness 1.5–10.5 m; commonly but intermittently exposed within or adjacent to unit Qpc in cliffs along the Nisqually River valley and mostly shown as map unit points.

We interpret unit Qpvl as deposits from lahars (diamicton), lahar run-outs (diamicton, gravel, sand), and hyperconcentrated flows (observed in postglacial equivalent unit Qvl: mostly sand, some gravel; commonly pumiceous). Some cliffs reveal lahars at multiple levels. For instance, at least two and probably four lahars are visible at RM28.34R (Fig. 2A). Boulders scattered in some active-channel reaches of the Nisqually River appear to be lag deposits of lahar units Qvl and Qpvl that were eroded by the river. Unit Qpvl commonly rests on sharp, conformable to unconformable and locally erosional contacts with underlying unit Qpc. Contacts with overlying unit Qpc commonly appear conformable. Clast compositions and modern geography suggest provenance from Mount Rainier and its vicinity. Interbedding indicates that the age of unit Qpvl is similar to that of unit Qpc, likely ranging from >1 Ma (for instance, at age sites GD 8–10, RM16.7L) to late MIS 3 (see unit Qpc). Some large lahars during MIS 5 may be associated with Mount Rainier's Sunset Amphitheater tephra, which Sisson and others (2019) associate with lahar run-out deposits on Ketron Island downstream of the map area.

## Late to Middle Eocene Northcraft Formation Volcanic Rocks

**Ev<sub>n</sub>** **Undivided igneous rocks (late to middle Eocene)**—Dark gray to medium gray lavas, mostly andesite and basaltic andesite, but ranging from basalt to rhyolite, basaltic trachyandesite, trachyandesite, dacite and trachydacite (see *Geochemistry*); interbedded with pale brown to brown, tan, and olive lahar deposits, pyroclastic tuff, flow breccia, and other volcanoclastic rocks. Undivided unit Ev<sub>n</sub> is mapped where subunits could not be separated. Radiometric ages were collected from seven samples of Northcraft Formation and are well within the combined range of Northcraft Formation ages reported nearby west of the map area (Polenz and others, 2021:  $45.80 \pm 0.07$  Ma to  $<38.4 \pm 0.5$  Ma) and elsewhere farther from the map area (Snively and others, 1958: late Eocene; Hagen 1987:  $38.8 \pm 1.9$  to  $32.7 \pm 1.5$  Ma). The new ages (see Table 2, Appendices B and C, and Data Supplement) are discussed below (see *Discussion*). Locally subdivided into:

**Ev<sub>b</sub><sub>n</sub>** **Basalt lava flows (late to middle Eocene)**—Basalt lava; black to very dark gray, poorly columnar, vesicular, glassy to slightly porphyritic. Unit Ev<sub>b</sub><sub>n</sub> consists of less than 10 percent phenocrysts, including 3–5 percent altered, euhedral plagioclase, 1–2 mm in size; trace to 1 percent clinopyroxene, <0.5 mm in size; trace to 1 percent olivine with pyroxene rims, <0.5 mm in size. The groundmass is 70–75 percent clear glass with amorphous yellowish green clay, 7–10 percent black opaques, 7–10 percent plagioclase microlites, and 5–10 percent subhedral feldspar stubs. Unit Ev<sub>b</sub><sub>n</sub> was only observed in a small knoll northeast of Jonas Hill (geochemistry site G12). Unit Ev<sub>b</sub><sub>n</sub> in the map area is undated and considerably more mafic than the other lavas in the map area. It is surrounded by Quaternary glacial deposits and isolated from other bedrock exposures. We mapped this basalt as Northcraft Formation because other inselbergs of Northcraft Formation bedrock are common in the vicinity, and the Northcraft Formation also includes (dated) basalt in the adjacent Vail quadrangle located west of the map area (Polenz and others, 2021).

**Eva<sub>n</sub>** **Andesite and basaltic andesite flows (late to middle Eocene)**—Lava flows of mainly andesite, basaltic andesite, and less commonly trachyandesite and basaltic trachyandesite (see *Geochemistry*); may locally include minor, interbedded volcanoclastic rocks; dark gray to dark olive gray; dense where unweathered, very dense and hard where aphanitic; porphyritic with plagioclase



**Table 2.** Summary of age analyses. Further sample and analysis information is in the appendices and Data Supplement.

Sample	Material	Map Unit	Method	Notes	Age
GD1	sand	Qpc	Infrared-stimulated luminescence	Alluvial sand from ancestral Nisqually River.	142.6 ±38.2 ka
GD2	sand	Qpc	Infrared-stimulated luminescence	Alluvial sand from ancestral Nisqually River. Sample collocated with GD3 at RM17.1R, 420 m east of map area and thus not shown on map plate.	187.0 ±58.6 ka
GD3	sand	Qpc	Detrital Zircon	Maximum depositional age: weighted mean of 60 $^{238}\text{U}/^{206}\text{Pb}$ ages at young end of spectrum; youngest age excluded. Sample collocated with GD2 at RM17.1R, 420 m east of map area and thus not shown on map plate.	1.02 ±0.01 Ma
GD4	sandstone	Evc <sub>n</sub>	Detrital Zircon	Maximum depositional age from sandy matrix of conglomerate: weighted mean of 69 $^{238}\text{U}/^{206}\text{Pb}$ ages at young end of spectrum.	36.95 ±0.07 Ma
GD5	plagioclase	Qpvl	$^{40}\text{Ar}/^{39}\text{Ar}$	Plagioclase in a dacite clast from a lahar deposit about 33–38 m above river provides plagioclase crystallization age (max. age for lahar).	259 ±14.8 ka
GD7	plagioclase	Qpvl	$^{40}\text{Ar}/^{39}\text{Ar}$	Plagioclase in a dacite clast from a lahar deposit about 33–38 m above river provides plagioclase crystallization age (max. age for lahar).	390.1 ±16.9 ka
GD6	plagioclase	Qpvl	$^{40}\text{Ar}/^{39}\text{Ar}$	Plagioclase in a basaltic andesite clast from a lahar about 33–38 m above river provides plagioclase crystallization age (max. age for lahar).	331.4 ±21.7 ka
GD9	andesite	Qpvl	$^{40}\text{Ar}/^{39}\text{Ar}$	Groundmass of andesite clast from same lahar as GD8 and GD10. Analysis provides eruption age (max. age for lahar).	1.191 ±0.004 Ma
GD10	plagioclase	Qpvl	$^{40}\text{Ar}/^{39}\text{Ar}$	Plagioclase in dacite clast from same lahar as GD8 and GD9. Analysis provides plagioclase crystallization age (max. age for lahar).	1.20 ±0.03 Ma
GD8	andesite	Qpvl	$^{40}\text{Ar}/^{39}\text{Ar}$	Andesite groundmass of a clast from same lahar as GD9 and GD10. Analysis provides eruption age (max. age for the lahar).	1.162 ±0.008 Ma
GD16	andesite	Eva <sub>n</sub>	$^{40}\text{Ar}/^{39}\text{Ar}$	Andesite groundmass; age resembles others from same unit (Polenz and others, 2021) but lab notes a discordant age spectrum and cautions the age does not mean much.	43.5 ±0.09 Ma
GD15	andesite	Evc <sub>n</sub>	$^{40}\text{Ar}/^{39}\text{Ar}$	Groundmass of an andesite bomb clast in a lahar deposit provides crystallization age (max. constraining age for lahar). Same lahar as GD14, but different clast.	42.8 ±0.1 Ma
GD11	plagioclase	Evd <sub>n</sub>	$^{40}\text{Ar}/^{39}\text{Ar}$	Plagioclase in dacite provides plagioclase crystallization age for columnar dacite that cooled against a trachydacite valley wall (analyzed in sample GD12).	40.76 ±0.15 Ma
GD13	dacite	Evd <sub>n</sub>	$^{40}\text{Ar}/^{39}\text{Ar}$	Dacite groundmass provides eruption age.	41.36 ±0.09 Ma
GD14	plagioclase	Evc <sub>n</sub>	$^{40}\text{Ar}/^{39}\text{Ar}$	Plagioclase in basaltic andesite bomb clast from a lahar deposit provides a plagioclase crystallization age (max. age for lahar). Same lahar as GD15, but different clast.	42.20 ±0.25 Ma
GD12	trachydacite	Evd <sub>n</sub>	$^{40}\text{Ar}/^{39}\text{Ar}$	Trachydacite groundmass provides eruption age for a valley wall against which a nearly aphyric dacite flow cooled. That flow was analyzed in sample GD11.	40.90 ±0.11 Ma

up to 4 mm except where locally aphanitic; blocky. Aphanitic samples are trachytic—comprised of parallel aligned microlites and intersertal glass. Unit Eva<sub>n</sub> is mapped only in the valley south of Jonas Hill, where it is overlain by unit Evc<sub>n</sub>. Andesitic ridge-top lava flows west of the map area (Polenz and others, 2021) and just south of the map area reveal a pattern of unit Eva<sub>n</sub> underlying and overlying volcanoclastic deposits of unit Evc<sub>n</sub>. Polenz and others (2021) also found that west of the map area, andesite ages from ridge top flows above unit Evc<sub>n</sub> overlap within error ages from valley floor flows below unit Evc<sub>n</sub>. This implies that the intervening stack of Evc<sub>n</sub> accumulated within the time covered by the age overlap and suggests that there is little age difference

between unit Eva<sub>n</sub> above and below unit Evc<sub>n</sub>. New ages from Northcraft andesite in the map area include a 43.50 ±0.09 Ma  $^{40}\text{Ar}/^{39}\text{Ar}$  total fusion age from a flow at age site GD16—which the lab cautions is not very meaningful due to a discordant age spectrum. See *Discussion* for new ages from this subunit.

#### Evc<sub>n</sub>

**Volcanoclastic deposits (late to middle Eocene)**—Varied volcanoclastic deposits, including: (1) bouldery diamictite with clasts of mostly andesite (see geochemistry sites G19–24) and less commonly dacite (for instance at geochemistry site G26); mostly lahar deposits but ranging to pyroclastic block and lapilli-ash flow tuff; (2) within unbedded lahars, rare channel

fills of tuffaceous, immature volcanic-lithic sandstone and sandy, rounded-pebble conglomerate that locally contains petrified wood (for instance in a landslide block 90 m southeast of geochemistry site G26); (3) centimeter- to decimeter-scale, planar and graded, moderately sorted beds of volcanic lithic sandstone, siltstone, and angular pebble conglomerate with carbonized wood fragments, such as at clast count site C8; (4) light brown, tan, or olive, unbedded to poorly bedded, moderately to poorly sorted and mostly matrix-supported, devitrified crystal-lithic vitric lapilli-ash flow tuff, for instance in the NW1/4, SW1/4, Sec. 4, T15N, R02E; (5) radially-fractured volcanic bombs (observed at Jonas Hill). Clast weathering ranges from fresh to highly varied within individual outcrops. Unit Evc<sub>n</sub> is mostly unwelded but locally ranges to moderately welded. Channel fill sandstone is coarse and granular, usually poorly sorted, channels themselves are a few meters wide, and bed thicknesses in both channel fill and planar beds range from centimeters to decimeters. Abundant blocks range from 0.1 m to more than 1 m in diameter and are sub-rounded in the tuff diamict, with local surface chatter-marks, but angular to subangular in pebble conglomerate. Tuffaceous beds contain angular lapilli and devitrified ash while sandstone beds range from clay-rich to clay-free.

Unit Evc<sub>n</sub> forms a band of cliffs and low prominences on the steep slopes south and east of the top of Jonas Hill, and prominent cliffs farther east of Shell Rock Ridge. It is 180 m thick south of Jonas Hill, 150 m thick at Jonas Hill, and at least 105 m thick at Shell Rock Ridge. The unit is notably landslide-prone. Weathering increases upsection in the lahar deposits, especially near the western map edge. Weathering is particularly prevalent in the upper 60 m where porphyritic andesite blocks are progressively reduced, first to porphyritic clay ghosts in a saprolite matrix, and finally, in the uppermost exposures, to a mass of homogeneous clay. Weathering is less pronounced farther east in the Shell Rock Ridge area. Varied clast weathering suggests a varied provenance. See *Discussion* for new ages from this subunit.

Evd<sub>n</sub>

**Dacite (late to middle Eocene)**—Lava flows of dacite to trachydacite (see *Geochemistry*); pale reddish purple and medium dark to dark gray, platy to blocky. Narrow, sub-millimeter

bands of very finely crystalline (<0.1 mm) magnetite and hematite lend a pale, reddish purple tinge to the rock and accentuate color banding and colored partings unique to this unit. Petrography reveals parallel alignment of plagioclase microlites that contributes to mineralogic banding at many locations. Dull, white, elongate feldspar phenocrysts 1–5 mm in length comprise 5–7 percent of the rock, surrounded by gray to pale, reddish-purple groundmass with an earthy luster. Sparse black pyroxene crystals 1–2 mm in length comprise less than 1 percent of the rock. Unit Evd<sub>n</sub> is widely exposed on the western flank of Shell Rock Ridge and farther south and west. Smaller, isolated exposures of dacite, some elongate, occur in low hills in the north halves of sections 31 and 32, T16N, R02E. Farther west at geochemistry site G15, a nearly aphyric dacite flow in a quarry on the west side of Jonas Hill forms 10–15-cm-wide, nearly perfectly hexagonal dark gray to black, glassy columns that weather tan. This flow rests against a lighter-colored, steep trachydacite slope on the east side of the quarry (geochemistry site G14). Three new <sup>40</sup>Ar/<sup>39</sup>Ar ages on dacite from the map area reveal: a 40.76 ± 0.15 Ma plagioclase crystallization age (age site GD11) from the columnar dacite flow at G15 is within error of a 40.9 ± 0.11 Ma eruption age on trachydacite groundmass (age site GD12) from the adjacent slope at geochemistry site G14. Farther east at Shell Rock Ridge (geochemistry site G25), <sup>40</sup>Ar/<sup>39</sup>Ar analysis of dacite groundmass yielded a plateau age of 41.36 ± 0.09 Ma (age site GD13).

## DISCUSSION

### Eocene Bedrock

The Northcraft Formation was actively sampled to determine the composition and age of its subunits. Samples were selected from andesite lava, andesitic boulders in lahars, dacite lava flows, and ashy matrix from a volcaniclastic conglomerate. Seven new Northcraft Formation radiometric ages ranged from a 43.50 ± 0.07 Ma <sup>40</sup>Ar/<sup>39</sup>Ar total fusion age on andesite flow groundmass (age site GD16—age questionable due to a discordant age spectrum) to a <36.95 ± 0.07 Ma maximum constraining age from U/Pb analysis of detrital zircons from volcaniclastic conglomerate (age site GD4) (Table 2; Appendices B and C, and Data Supplement).

This project includes a new <sup>40</sup>Ar/<sup>39</sup>Ar total fusion age from a Northcraft andesite flow of 43.50 ± 0.09 Ma from a flow at site GD16. Although this age is suspect due to a discordant age spectrum, it is within the range of ages reported by Polenz and others (2021). Two clasts, of andesite and basaltic andesite, (age sites GD15 and GD14, respectively) are from a bouldery lahar deposit in unit Evc<sub>n</sub> and yielded ages of 42.80 ± 0.1 and

42.20 ± 0.25 Ma, respectively. Together with the suspect lava flow age, all three ages are within the roughly 42.5–46 Ma range of lava ages that Polenz and others (2021) documented west of the map area. The younger of the two  $^{40}\text{Ar}/^{39}\text{Ar}$  ages from clasts in the lahar deposit at age sites GD14–15 provides a <42.20 ± 0.25 Ma maximum constraining age for lahar deposition at that site (Tables 2 and A3).

Three new  $^{40}\text{Ar}/^{39}\text{Ar}$  ages on dacite from the map area cluster around 41 Ma, suggesting that the dacite eruptions centered in the vicinity of Shell Rock Ridge may have been short-lived amid several million years of Northcraft volcanism. This is somewhat younger than the 42.5–46 Ma age range reported for less felsic lavas. There is field evidence, however, that dacite volcanism was active longer than the cluster of dates at 41 Ma suggests, because of the presence of rare, but distinctive, dacite clasts within the andesite-dominated lahar deposits. Although ages overlap within error at age sites GD11 and GD12, we interpret the dacite at GD11 as a younger flow that cooled against an older trachydacite valley wall (GD12) because that relationship is suggested by field exposures, and geochemical traits suggest separate flows for the corresponding geochemistry sites G15 (GD11) and G14 (GD12). Geochemical differences include >2 percentage points difference in  $\text{SiO}_2$  content, a still-greater difference in  $\text{Al}_2\text{O}_3$  content, and 330 ppm compared to 680 ppm Ba.

Andesitic ridge-top lava flows west of the map area (Polenz and others, 2021) reveal a pattern of unit  $\text{Eva}_n$  both underlying and overlying volcanoclastic deposits of unit  $\text{Evc}_n$ . The andesite ages that Polenz and others (2021) documented west of the map area in ridge-top flows above unit  $\text{Evc}_n$  overlap in age, within error bars, with ages from valley floor flows below unit  $\text{Evc}_n$ . This suggests that the ages of the lava flows on the ridge tops and the valley floors are basically the same, and implies that the intervening stack of  $\text{Evc}_n$  west of the map area accumulated within a short time. We found a similar pattern of andesite flows bracketing unit  $\text{Evc}_n$  in the current map area at and south of Baumgard Hill, where volcanoclastic deposits are sandwiched between andesite flows, albeit the upper andesite flows are just south of this project's map boundary.

Farther north, in the lowlands, at age site GD4 (Sec. 34, T16N, R2E), no bracketing flows are exposed and detrital zircon age analysis from sandy conglomerate matrix, that we field-interpreted as alluvial deposits, yielded a <36.95 ± 0.72 Ma maximum constraining age—younger than all other known Northcraft ages in or west of the map area. The sample at GD4 had been previously mapped as Miocene Mashel Formation (Noble and Wallace, 1966; Schasse, 1987), but based mainly on a lack of post-Eocene zircons at GD4, we dismiss a Miocene age for deposits in the lowlands of the map area, for now. Because unit  $\text{Evc}_n$  at GD4 (and nearby exposures of tuff, sand, and conglomerate) is also on average finer-grained and more commonly bedded than unit  $\text{Evc}_n$  elsewhere in the map area, we further reason that these northern exposures may be derived from a younger, more distal source. However, that inference is not compelling, and we note a close resemblance between the mostly coarse, bouldery, blocky (and likely proximal) lahar deposits of unit  $\text{Evc}_n$  farther south in the map area and clast lithologies at age site GD4 (clast count C7). Other similarities include inclusions of petrified wood fragments, and exposures

of bouldery lahar deposits that we observed along the Deschutes River channel near age site GD4.

The ages and mapped distribution of unit  $\text{Evc}_n$  imply a several-km-wide, >180 m-thick volcanoclastic section sourced from a nearby, tall, steep stratovolcanic edifice(s) that may have produced volcanoclastic events over several million years. Transport of these coarse clastic deposits was primarily by lahars of various temperatures. Ash flow deposits are present but not a major constituent in the map area. Periods of quiescence between lahars allowed for channelization and rounding of pebbles atop lahar deposits before the next lahar arrived. Petrified wood, while not abundant, indicates that enough time passed between formative events to allow trees to grow on the flanks of the ancient volcano(es). This suggests that the volcano(es) underwent periods of growth and partial collapse, a pattern typical for stratovolcanoes.

## Quaternary Sediment

### LATE PLEISTOCENE GLACIAL AND NONGLACIAL SEDIMENT

Sediment in the map area includes (1) drift from Cordilleran ice advances (often termed “northern-sourced”) and (2) Cascade Range-sourced sediment, derived mostly from Mount Rainier and nearby areas (Table 1). Vashon Drift units are northern-sourced and can be identified by selected rock and mineral constituents from plutons and metamorphic rocks in Washington's north Cascades, the San Juan Islands, and the Coast Mountains of British Columbia (Polenz and others, 2019). However, in the east half of the Puget Lowland, drift from Cordilleran ice advances deposited sediment that was sourced almost exclusively from the Cascade Range, such that diagnostically northern-sourced constituents commonly comprise only trace quantities. Cascade Range-sourced deposits include some post-glacial and all pre-Vashon sediment we observed. Cascade Range-sourced sediment assemblages in the map area are illustrated by clast counts C4, C5, and C6 (Data Supplement). Clast counts C1 and C3 illustrate northern-sourced drift assemblages in the map area. Clast count C2 illustrates that some assemblages are mixed, at least in the northern part of the map area. Clast counts C7 and C8 illustrate Northcraft Formation volcanoclastics.

### VASHON DRIFT

Vashon glacial sediment and associated landforms define the landscape in the map area, which is appreciably interrupted only by post-glacial incision of the Nisqually River valley, a veneer of post-glacial alluvium in the valley floors of the Deschutes and Nisqually Rivers, and exposures of Northcraft Formation within the mountainous, southernmost 3 km of the map area. The distribution of glacial sediment units mostly corresponds to associated landforms: chaotically bumpy and kettled surfaces on both sides of the Deschutes River valley mark terminal moraines (or landslides). North of the terminal moraine, lodgment till is associated with northeast–southwest-aligned, elongate hills (drumlins) and parallel troughs (flutes) with surfaces smoothed by the southwestward movement of glacial ice. Skinny, elongate, worm-like winding hills mark eskers. Randomly scattered, closed depressions (kettles), eskers, and relict channels and

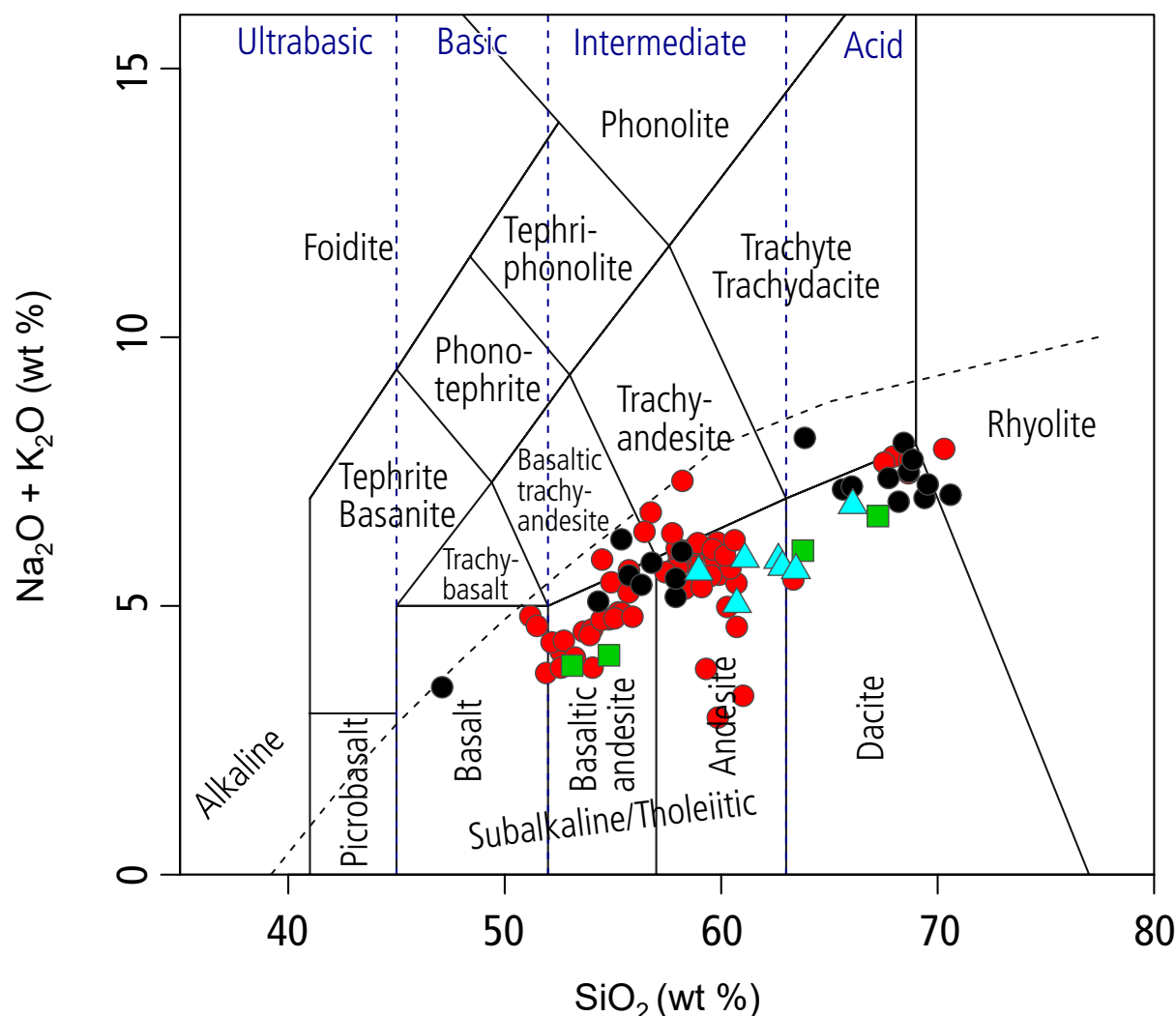


**Figure 3.** Total alkalis versus silica plot (Le Bas and others, 1986) with Northcraft data from this study (black circles) and Polenz and others (2021) (red circles). Note also the compositional gap between 62–66 wt. %  $\text{SiO}_2$ . Also plotted are clasts from Quaternary lahar deposits in the Nisqually River valley, where blue triangles are from a site at the eastern map edge and green squares from farther downstream near the northeastern map corner.

valleys with little or no modern stream activity, all of which are commonly superimposed either on flutes and drumlins or on gently irregular to flat surfaces, signal areas of stagnant ice deposits (unit Qgic). Flat to gently sloping surfaces, commonly stepped in terrace flights, and (or) with relict channel forms, mark glacial outwash deposits. Despite their surficial prominence, the glacial landforms and Vashon Drift generally seem to form only a thin veneer in the map area, typically 2–15 m thick.

The northern-sourced lithologic content of Vashon Drift in the map area (Table 1) is heavily diluted by andesite-rich Cascade Range-sourced material, such that diagnostically northern-sourced constituents (Table 1) are commonly found only in trace quantities. The only observed exception to this pattern is ablation and lodgment till at the top of Jonas Hill, where abundant, northern-sourced constituents are readily apparent even in small exposures. We attribute this to the hilltop setting, where Vashon Drift had to be sourced entirely from allochthonous supraglacial and englacial debris, unaffected by addition of Cascade Range-derived sediment from subglacial erosion and synglacial Cascade Range-sourced runoff.

Till at more than 1,100 ft elevation atop Jonas Hill provided our control for showing the Vashon ice limit at close to 1,000 ft along the north-facing slope near the southern map edge, where Vashon Drift deposits are common only below about 700 ft elevation. The elevation of the ice limit line is therefore inferred.

### LAHAR AND LAHAR RUN-OUT DEPOSITS

Lahar and lahar runout deposits, both post-glacial (unit Qvl) and pre-Vashon (unit Qpvl), abound along the Nisqually River valley. Their observed thicknesses up to 10.5 m and the ability of the lahars to move boulders up to >3 m in diameter indicate large, energetic events capable of substantially changing the valley floor in the map area—about 75 to 88 km down-valley of Mount Rainier. This suggests that future lahars can also catastrophically impact downstream infrastructure, including Interstate 5. However, lahar frequency remains mostly unassessed. Assuming that large lahars are formative events within the Nisqually River system, their deposits may be over-represented in the alluvial section along the valley walls, and age control data from the lahars and surrounding alluvium remains sparsely scattered, with ages in the pre-Vashon section ranging from  $26 \pm 5$  ka to about 1,000 ka



**Figure 4.** Alkali-Iron-Magnesium ternary plot (AFM diagram) (Irvine and Baragar, 1971) showing that the majority of Northcraft and lahar clast samples classify as calc-alkaline. Symbols are the same as in Figure 1.

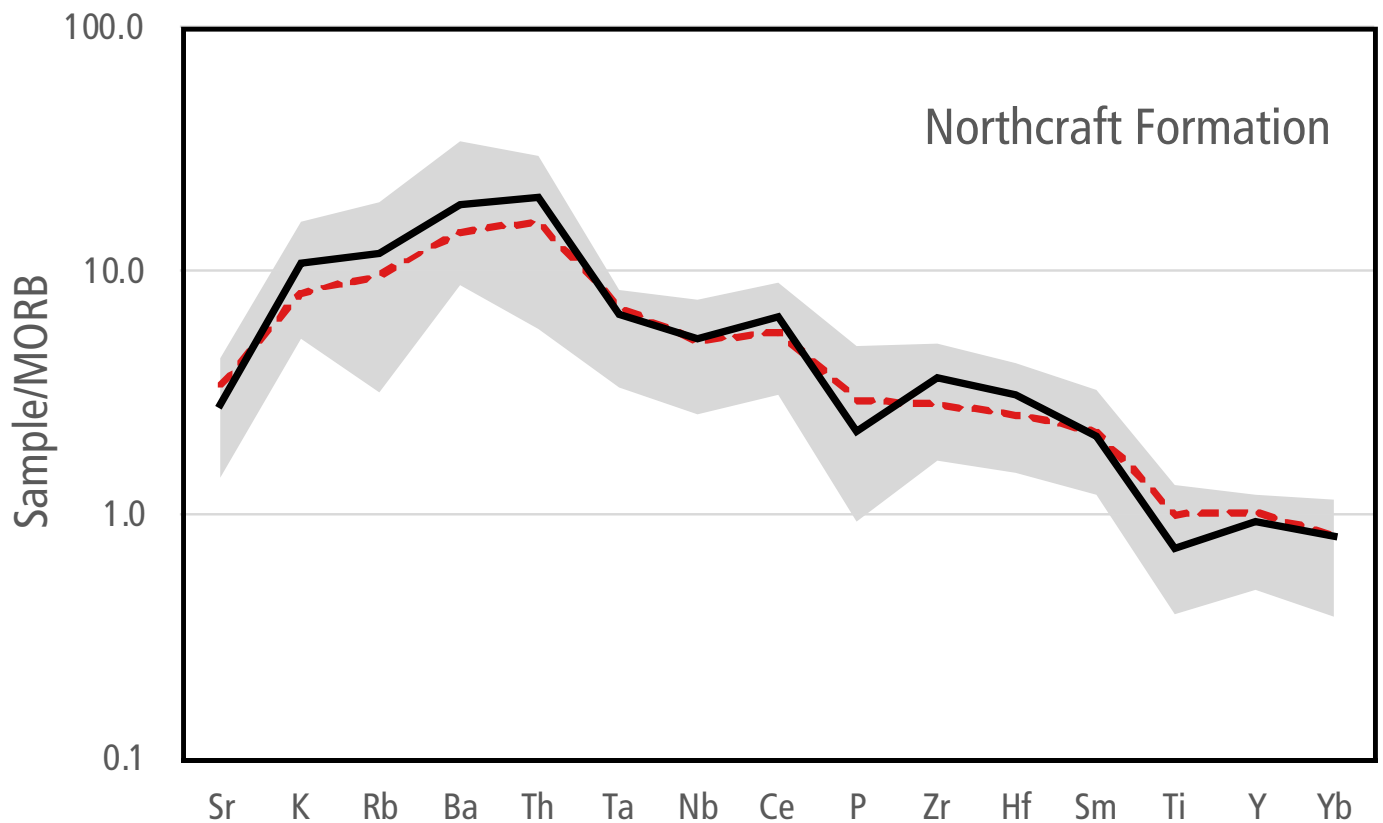
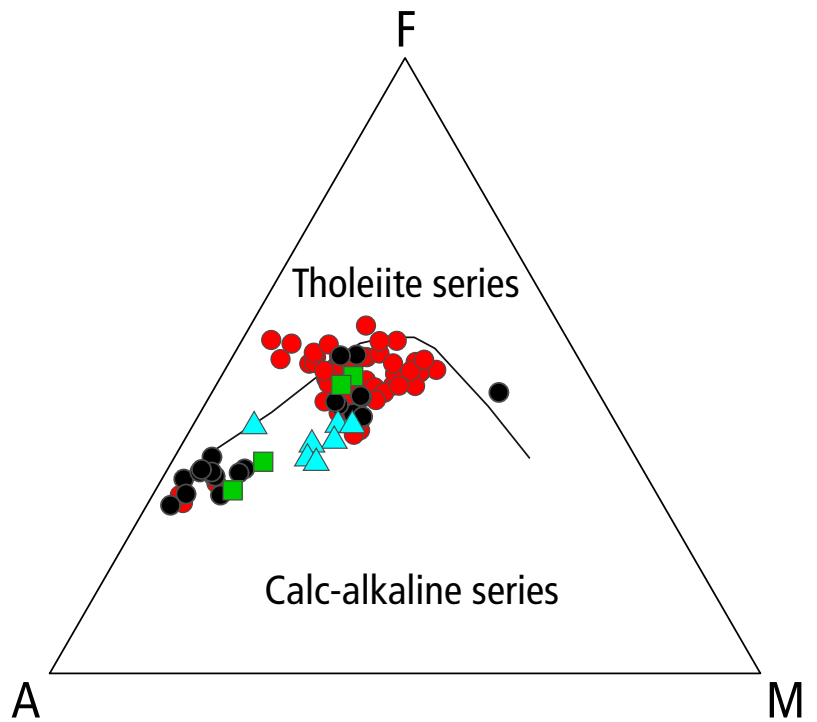


**Figure 5.** MORB-normalized spider diagram showing K-Rb-Ba-Th enrichments and Ta-Nb depletions characteristic of subduction-related magmas. Shaded region outlines the range for 20 Northcraft samples in this study. Solid lines are averages for this study (black) and Northcraft samples west of the map area (red, from Polenz and others, 2021). Depletions in P and Ti reflect fractionation of apatite and ilmenite in some samples. Data normalized to the MORB values of Sun and McDonough (1989).

(see unit Qpc). Sisson and Vallance (2008) noted that Mount Rainier produced at least 10–12 eruptions within the past 2,600 years, each of which likely included “multiple explosive events spanning months to possibly years” (p. 22), and these “eruptions were penecontemporaneous with far-traveled lahars” (p. 23). But many events can trigger lahars in the Nisqually River valley, from spontaneous collapse of unstable mountain flanks to rainfall events, seismic shaking, melting glaciers, and volcanic eruptions (Sisson and Vallance, 2008). Scott and others (1995) suggested that post-glacial lahars large enough to leave a notable deposit in the map area have been rare (>500 yr recurrence interval).

## Whole Rock Geochemistry

Whole rock chemical analyses were determined on 31 igneous samples: 20 collected from bedrock outcrops of the Northcraft Formation in the Lake Lawrence quadrangle (geochemistry sites G12–G24), and 11 taken from clasts in two Quaternary lahar deposits along the sidewalls of the Nisqually River valley in the McKenna quadrangle (geochemistry sites G1–G4 at RM28.34R near the northwest map corner in JBLM and G5–G11 at RM16.74L along the eastern map edge 1 km south of where the Nisqually River enters the map area).

The Northcraft samples range from basalt to rhyolite (47.1–70.6 wt. %  $\text{SiO}_2$ ; 10.1–0.4 wt. %  $\text{MgO}$ ) but most classify as basaltic andesite, andesite, or dacite (Fig. 3). The suite is bimodal, with the dacite and rhyolite (geochemistry sites G13–G15, G17, G25–G31) being separated from the other lavas (geochemistry sites G12, G16, G18–G24) by a compositional gap between 58–64 wt. %  $\text{SiO}_2$ . Although among the samples from the map area this gap resembles the Daly Gap observed in bimodal arc volcanic settings elsewhere (Dufek and Bachman, 2010), the gap shrinks when Northcraft samples from west of the map area (Polenz and others, 2021) are included (Fig. 3). This suggests that additional Northcraft Formation samples may reveal the unit to not be bimodal. All samples classify as subalkaline (Fig. 3) and calc-alkaline (Fig. 4), are moderately LREE-enriched (average  $\text{La/Yb}_n = 7.3$ ) and have high field strength element (Ta, Nb) depletions on a MORB-normalized spidergram (Fig. 5). These traits are diagnostic of subduction-related magmas and are consistent with interpretation of the Northcraft Formation as an early expression of the Cascade arc (Hagen, 1987; Phillips and others, 1989; Polenz and others, 2021). In general, major and trace element compositions of these samples overlap with Northcraft analyses from the adjacent Tenalquot Prairie and Vail quadrangles, although we sampled more dacite in this study area (Figs. 3–5). In addition, glassy basalt at geochemistry site G12 is significantly more primitive (10.1 wt. %  $\text{MgO}$ , Mg number = 61) than any previously reported Northcraft lava, although its low Cr content (10 ppm) indicates that it has undergone (chromite-) fractionation and precludes geochemistry site G12 being parental to the more differentiated Northcraft samples analyzed in this study.

The clasts from Quaternary lahars include calc-alkaline basaltic andesite, andesite, and dacite (Figs. 3–4) ranging from 53–67 wt. %  $\text{SiO}_2$ . With the exception of dacite at geochemistry site G9, which is also more altered, all of the clasts have adakite traits, including  $\text{Sr} > 400$  ppm,  $\text{Sr/Y} > 20$ ,  $\text{Yb} < 1.8$  ppm, and high  $\text{La/Yb}_n$  (average = 9.8). There are also subtle trace element

contrasts between clasts from the two lahars, where those from RM28.34R (geochemistry sites G1–G4; Fig. 2) have higher Nb, Hf, Zr, Ba, and lower Sr. The clasts are broadly similar in composition to lavas from Mount Rainier and vicinity (Sisson and others, 2014), but the available data are insufficient to establish correlation to any particular geologic unit. However,  $^{40}\text{Ar}/^{39}\text{Ar}$  ages for clasts from the upstream lahar site (~1.2 Ma; age sites GD8–GD10 and geochemistry sites G5–G7) are close to those of clasts in the Lily Creek Formation (1.2–1.3 Ma) that were sourced from an ancestral Mount Rainier (Pringle, 2008). Similarly,  $^{40}\text{Ar}/^{39}\text{Ar}$  clast ages from the downstream lahar site (about 260–390 ka, age sites GD5–GD7; geochemistry sites G1–G3) are close to those of an episode of heightened activity on the southwest flank of the present-day edifice of Mount Rainier (Pringle, 2008).

## Geophysics and Structures

Northwest-striking, tentatively mapped faults across the map area coincide with the transition from the Puget Lowland southward into the foothills of the western Cascades. The main drainages and ridges south of the map area similarly trend northwest, as do the Deschutes and Nisqually Rivers across the map area, and we suspect that these orientations express structural control. However, the faults we show on the map and cross-section are inferred from potential-field map patterns (Fig. M1A) and our 2D forward modeling of aeromagnetic and densely spaced gravity data along model line X–X', which includes Cross Section A–A' in the map area (see our preferred model in Fig. M1B). Like modeling results west of the map area (Polenz and others, 2021), data we model here require faulted offset between mafic igneous basement (Crescent Formation in Fig. M1B) and the overlying western Cascade arc rocks (interbedded flows, andesite flows, and dacite in Fig. M1B) at the Olympia fault (see *Overview of Regional Structure*). This fault provides a good fit of a major, northwest-trending, steep and high-amplitude, northeast-down gravity gradient (marked by max spots, ‘OF’ in Fig. M1A). The large magnitude of the gradient requires the part of the Tacoma basin captured by the model extent to be largely filled with low-density material that we interpret as volcanics and sediment. Based on our density measurements on samples from this project (Data Supplement) and nearby WGS projects (WGS unpublished records), we assumed  $\rho$  of 2,210; 2,380; and 2,290  $\text{kg/m}^3$  for volcanoclastics, andesite, and sedimentary rocks, respectively, compared to 2,880  $\text{kg/m}^3$  for Crescent Formation. This large gradient has two sections in the high-resolution profile data along model line X–X', each with a different slope; the steepest section is positioned northeast of the center of the gradient (‘OFN’ in Figs. M1A, B). This suggests a near-surface fault at this location, which we interpret as a strand of the Olympia fault.

Our modeling confirms that voluminous low-density, highly magnetic volcanics fill a large area of the Tacoma basin adjacent to the Olympia fault. Aeromagnetic data strongly support scattered near-surface magnetic rocks (such as Northcraft Formation andesite) throughout the hills southwest of the Tacoma basin, marked by many short-wavelength magnetic highs (‘MNV’ in Fig. M1A). A much broader, moderate amplitude aeromagnetic high over the Tacoma basin northeast of the Olympia fault (‘TBV’ in Fig. M1A, B) suggests a more deeply buried,

extraordinarily thick ( $>2,500$  m) package of highly magnetic rocks, with properties typical of the andesite in the region ( $\rho = 2,380$  kg/m<sup>3</sup>,  $\chi = 55 \times 10^{-3}$  SI). This package (“predominantly Northcraft andesite flows” in Fig. M1B; ‘TBV’ in Fig. M1A) may be interbedded with some less-magnetic tuffs and sediment, given that basins tend to collect such materials, but the top of the highly magnetic rock must be at most  $\sim 300$  m below the surface within the basin. One aeromagnetic high over the basin (‘AV’ in Fig. M1A) is large enough amplitude that a locally thick pile of subsurface magnetic volcanics is necessary in our model to match the magnetic data. The shape of this pile in cross section is flexible in our models, but given the shape of AV in Fig. M1A, we hypothesize it is a vent that erupted some or all of the magnetic rocks responsible for the TBV anomaly. The TBV anomaly has a rather linear northeastern edge, which suggests that this edge might be fault-controlled; its orientation is consistent with northeast–southwest extension inferred by Snively and others (1958).

Aeromagnetic anomalies suggest multiple sub-parallel fault strands at shallow depth within the Olympia fault. Aeromagnetic data filtered to enhance short-wavelength anomalies due to near-surface sources reveal several semi-continuous northwest–southeast trending aeromagnetic gradients on either side of the gravity max-spots at the location of the Olympia fault (which we display as lineaments on the geophysical map; Fig. M1A). Their shallow geophysical source, sub-parallel orientations, and stepped distribution suggest these lineaments show the positions of faults in the near-subsurface (upper  $\sim 200$  m). A short-wavelength gravity low that is collocated with the southernmost lineament crossing the model line (OFMS in Figs. M1A, B) is strong evidence for low density, weakly magnetic volcanoclastics mapped at the surface at this location, filling the topography under the southwestern end of the geophysical model. However, the steep, high-amplitude magnetic gradient at this location suggests a sharp boundary (most likely a fault) with strongly magnetic rocks to the southwest, which we interpret as the surface position of the main strand of the Olympia fault. The aeromagnetic lineaments also bracket a linear, low magnetic anomaly (GML in Figs. M1A, B). The only rock type in the region that could create such an aeromagnetic low collocated with low gravity is a thick package of volcanoclastic or sedimentary rock, which we interpret as a small graben on the northeast side of the main Olympia fault (OFMS in Figs. M1A, B). In this context, we interpret the lineaments as faults within an Olympia fault zone. Though the positions of the faults at the surface are well-constrained geophysically, in terms of our geologic map scale, we show the faults as only inferred and note that both the faults and their offsets are less constrained at greater depth in the geophysical model because, from a geologic-conceptual perspective, we suspect that the volcanic units and sedimentary packages are more layered in the subsurface than our data can resolve. Blocks within the modeled graben tilt south because sparsely scattered strike and dip measurements from this study and Polenz and others (2021) suggest that in-place bedrock orientations generally include a gently south-dipping component. We note that abrupt thickness changes of volcanic rock packages across the faults indicate syn-eruption faulting or some component of oblique fault offset.

Based on our potential-fields modeling, we offer two models for the Olympia fault zone. Both models envision multiple surface fault strands converging at depth into a master fault. Our preferred model envisions a northeast-dipping normal Olympia master fault with a dacite vent introducing thick, subsequently faulted dacite into the graben (DI in Fig. M1B; Cross Section A–A’). The second model envisions a vertical Olympia master fault, presumably a strike slip fault, with a negative flower structure near the surface locally resulting in a graben similar to that in the normal fault model (Fig. M1C). In both models, the offset of the dacite block and juxtaposition of the dacite ( $2,470$ – $2,510$  kg/m<sup>3</sup>) and volcanoclastics ( $2,210$  kg/m<sup>3</sup>) along fault OFN are very well constrained by the gravity data because only these two rock types (which are the most and least dense rocks measured in the region) offer enough density contrast to model the gravity anomaly at this location. Other aspects of the geometry of the dacite, especially below  $600$  m depth, are speculative, except for the considerable dacite volume along the Olympia fault, which is necessary to fit the gravity data in the normal fault model. The vertical fault model with a flower structure in the near-surface (Fig. M1C) lacks a dacite vent but retains dacite in the upper  $\sim 2$  km. It fits the geophysical data equally well. Both models are consistent with (but do not require) the suggestion by Polenz and others (2021) that major northeast-down offset along the Olympia fault ended no later than deposition of the Eocene Northcraft Formation. We suggest this because we have encountered no evidence of post-Northcraft volcanic rocks along the fault, but the geophysical data require near-surface volcanics filling the Tacoma basin to within  $300$  m of the surface just northeast of the Olympia fault.

Our map and cross-section A–A’ are based on the normal fault model because (1) our field observations of abundant dacite suggest proximity to a dacite vent; (2) whereas northeast-down offset (accommodated in both models) is consistent with the presence of the Tacoma basin northeast of the Olympia fault zone, we lack compelling evidence for strike-slip; (3) we interpret at least one northwest-trending aeromagnetic high in this area (OFI in Fig. M1A) as a fault-parallel intrusion (as previously suggested west of the map area by Polenz and others, 2021). In particular, the wide intrusion needed to model anomaly AV (Fig. M1A) suggests availability of abundant accommodation space in the minimum compression direction, consistent with broader, regional(?), northeast-oriented extension. However, we think that at least some strike-slip offset is also likely in the Olympia fault zone, mainly because anomalies in both gravity and aeromagnetism yield curvilinear max spot clusters with gaps and offsets between them. If the curvilinear max spot clusters are correctly interpreted as indicators of near-surface faults, then their discontinuous map pattern (aeromagnetic lineaments and gravity max spots in Fig. M1A) is typical of faults in strike-slip settings. Strike-slip tectonics could also accommodate—perhaps better than normal faulting—subsurface unit thickness changes across fault strands in both models. Strike-slip tectonics might also accommodate fault-parallel volcanic intrusions in pull-apart basins within the fault zone. Finally, at least at a regional scale, modern western Washington stress and strain generally include north–south or northeast–southwest compression or transpression, which are compatible with strike-slip tectonics

but not with our northeast-extensional normal fault model. Our inference of northeast extension would therefore require either that the Olympia fault zone was rotated after major normal offset, or that it responded to a stress field that probably is no longer present, whereas a strike-slip fault zone could remain active in the modern environment.

## SUGGESTIONS FOR FURTHER STUDY

- Systematic search of peat bogs near the Vashon ice limit to seek  $^{14}\text{C}$  data to better constrain the timing of the Vashon glacial maximum.
- Olympia fault—additional potential-fields gravity data collection and modeling, especially at the linear northeastern edge of the TBV anomaly on our geophysics Figure M1 could help to develop a better understanding of the Tacoma basin fill material and what kind of faulting, if any, bounds this anomaly.
- Further evaluation of the age and distribution of the Mashel Formation—Cascade Range-sourced sediment identified as Miocene, based on fossil content. If widespread and appreciably thick in the Tacoma Basin near the Olympia fault, this unit would suggest Miocene basin deepening and therefore activity on the Olympia fault. Walters and Kimmel (1968) and Noble and Wallace (1966) suggested the unit in and near the map area, but our mapping revealed exposures of putative Mashel Formation to be Northcraft Formation at age site GD4 and Quaternary sediment at age sites GD2 and GD3. This suggests that Mashel Formation may be less voluminous than previously thought.
- Paleo-magnetic study to assess rotation of crustal fragments in the vicinity of the Olympia fault.
- Collect active (or passive?) seismic data across the Olympia fault between Yelm and the Cascades to better characterize fault geometries (and folds) and thicknesses and lateral thickness changes of subsurface rock packages.
- Detailed stratigraphy of sediment exposed along the Nisqually valley walls, with emphasis on ages, character, and distribution of lahar deposits to better evaluate lahar frequency and size.

## ACKNOWLEDGMENTS

We thank: Pat Pringle and Tim Walsh (both WGS retired) and Norman MacLeod (USGS retired) for fielding questions about prior mapping and other issues; Kevin Hansen (Thurston County) for hydrogeologic insights; Todd Lau for assessment of rock density and magnetic susceptibility; all WGS staff who provided suggestions, edits, and guidance; Weyerhaeuser for access to proprietary data; Weyerhaeuser, the city of Centralia, the Nisqually Land Trust, Joint Base Lewis–McChord, Wilcox Family Farms, and countless other landowners for land access, local knowledge, historical context, well records, and other information.

## WORKER CONTRIBUTIONS

K. Alexander headed up cross section development and GeMS data format compliance. M. Anderson performed geophysical data collection and modeling. F. Hladky carried out most bedrock geologic fieldwork and all petrography and clast counts, and he drafted some unit characterization pamphlet text. G. Legorreta Paulín provided Landsat data analysis. D. Miggins performed argon geochronology. M. Polenz functioned as project lead, drafted GIS features and the overall report, and led Quaternary geologic fieldwork. J. Tepper analyzed geochemistry, prepared the geochemical data supplement, and drafted the geochemical discussion.

## REFERENCES

- Barnes, D. F.; Oliver, H. W.; Robbins, S. L., 1969, Standardization of gravimeter calibrations in the Geological Survey: *Eos Transactions, American Geophysical Union*, v. 50, no. 10, p. 626–627. [<https://doi.org/10.1029/EO050i010p00526>]
- Black, L. P.; Kamo, S. L.; Allen, C. M.; Davis, D. W.; Aleinikoff, J. N.; Valley, J. W.; Mundil, Roland; Campbell, I. H.; Korsch, R. J.; Williams, I. S.; Foudoulis, Chris, 2004, Improved  $^{206}\text{Pb}/^{238}\text{U}$  microprobe geochronology by the monitoring of a trace-element-related matrix effect; SHRIMP, ID-TIMS, ELA-ICP-MS and oxygen isotope documentation for a series of zircon standards: *Chemical Geology*, v. 205, p. 115–140. [<https://doi.org/10.1016/j.chemgeo.2004.01.003>]
- Blakely, R. J.; Wells, R. E.; Weaver, C. S., 1999, Puget Sound aeromagnetic maps and data: U.S. Geological Survey Open-File Report 99-514, version 1.0 [<http://geopubs.wr.usgs.gov/open-file/of99-514/>]
- Blakely, R. J.; Sherrod, B. L.; Weaver, C. S., 2020, High-resolution aeromagnetic survey of the Centralia area, southwest Washington: U.S. Geological Survey data release. [<https://doi.org/10.5066/P9T4UC6W>]
- Booth, D. B.; Troost, K. G.; Clague, J. J.; Waitt, R. B., 2004, The Cordilleran ice sheet. In Gillespie, A. R.; Porter, S. C.; Atwater, B. F., editors, *The Quaternary period in the United States*: Elsevier, p. 17–43.
- Bretz, J. H., 1911, The terminal moraine of the Puget Sound glacier: *Journal of Geology*, v. 19, no. 2, p. 161–174. [<https://doi.org/10.1086/621826>]
- Bretz, J. H., 1913, Glaciation of the Puget Sound region: *Washington Geological Survey Bulletin* 8, 244 p., 3 plates. [[http://www.dnr.wa.gov/publications/ger\\_b8\\_glaciation\\_pugetsound.pdf](http://www.dnr.wa.gov/publications/ger_b8_glaciation_pugetsound.pdf)]
- Brocher, T. M.; Parsons, T. E.; Blakely, R. J.; Christensen, N. I.; Fisher, M. A.; Wells, R. E.; SHIPS Working Group, 2001, Upper crustal structure in Puget Lowland, Washington—Results from the 1998 Seismic Hazards Investigations in Puget Sound: *Journal of Geophysical Research*, v. 106, no. B7, p. 13541–13564. [<https://pubs.er.usgs.gov/publication/70023259>]
- Brown, N. E.; Hallet, Bernard; Booth, D. B., 1987, Rapid soft bed sliding of the Puget glacial lobe: *Journal of Geophysical Research*, v. 92, no. B9, p. 8985–8997. [<https://doi.org/10.1029/JB092iB09p08985>]
- Buckovic, W. A., 1979, The Eocene deltaic system of west-central Washington. In Armentrout, J. M.; Cole, M. R.; Ter Best, Harry, Jr., editors, *Cenozoic paleogeography of the western United States*: Society of Economic Paleontologists and Mineralogists Pacific Section, Pacific Coast Paleogeography Symposium 3, p. 147–163.
- Chang, Zhaoshan; Vervoort, J. D.; McClelland, W. C.; Knaack, Charles, 2006, U-Pb dating of zircon by LA-ICP-MS: *Geochemistry, Geophysics, Geosystems*, v. 7, p. Q05009. [<https://doi.org/10.1029/2005GC001100>]



- Clement, C. R.; Pratt, T. L.; Holmes, M. L.; Sherrod, B. L., 2010, High-resolution seismic reflection imaging of growth folding and shallow faults beneath the southern Puget Lowland, Washington State: *Bulletin of the Seismological Society of America*, v. 100, no. 4, p. 1710–1723. [https://doi.org/10.1785/0120080306]
- Crandell, D. R.; Miller, R. D., 1974, Quaternary stratigraphy and extent of glaciation in the Mount Rainier region, Washington: U.S. Geological Survey Professional Paper 847, 59 p., 2 plates. [https://doi.org/10.3133/pp847]
- Daneš, Z. F.; Bonno, M. M.; Brau, E.; Gilham, W. D.; Hoffman, T. F.; Johansen, D.; Jones, M. H.; Malfait, B.; Masten, J.; Teague, G. O., 1965, Geophysical investigation of the southern Puget Sound area, Washington: *Journal of Geophysical Research*, v. 70, no. 22, p. 5573–5580. [https://doi.org/10.1029/JZ070i022p05573]
- Drost, B. W.; Ely, D. M.; Lum, W. E., II, 1999, Conceptual model and numerical simulation of the ground-water-flow system in the unconsolidated sediments of Thurston County, Washington: U.S. Geological Survey Water-Resources Investigations Report 99-4165, 254 p. [http://pubs.er.usgs.gov/publication/wri994165]
- Dufek, Josef; Bachmann, Olivier, 2010, Quantum magmatism: Magmatic compositional gaps generated by melt-crystal dynamics: *Geology*, v. 38, p. 687–690. [https://doi.org/10.1130/G30831.1]
- Eddy, M. P.; Bowring, S. A.; Umhoefer, P. J.; Miller, R. B.; McLean, N. M.; Donaghy, E. E., 2016, High-resolution temporal and stratigraphic record of Siletzia's accretion and triple junction migration from nonmarine sedimentary basins in central and western Washington: *Geological Society of America Bulletin*, v. 128, no. 3/4, p. 425–441. [https://doi.org/10.1130/B31335.1]
- Eddy, M. P.; Clark, K. P.; Polenz, Michael, 2017, Age and volcanic stratigraphy of the Eocene Siletzia oceanic plateau in Washington and on Vancouver Island: *Lithosphere*, v. 9, no. 4, p. 652–664. [https://doi.org/10.1130/L650.1]
- Fiebelkorn, R. B.; Walker, G. W.; MacLeod, N. S.; McKee, E. H.; Smith, J. G., 1982, Index to K-Ar age determinations for the State of Oregon: U.S. Geological Survey Open-File Report 82-596, 40 p., 1 plate. [http://pubs.er.usgs.gov/publication/ofr82596]
- Finn, C. A., 1990, Geophysical constraints on Washington convergent margin structure: *Journal of Geophysical Research*, v. 95, no. B12, p. 19533–19546. [https://doi.org/10.1029/JB095iB12p19533]
- Finn, C. A.; Phillips, W. M.; Williams, D. L., 1991, Gravity anomaly and terrain maps of Washington: U.S. Geological Survey Geophysical Investigations Map GP-988, 5 sheets, scale 1:500,000. [https://doi.org/10.3133/gp988]
- Gabet, E. J.; Horwath Burnham, J. L.; Perron, J. T., 2016, Critiques of the seismic hypothesis and the vegetation stabilization hypothesis for the formation of Mima mounds along the western coast of the U.S.: *Geomorphology*, v. 269, p. 40–42. [https://doi.org/10.1016/j.geomorph.2016.06.032]
- Gower, H. D.; Yount, J. C.; Crosson, R. S., 1985, Seismotectonic map of the Puget Sound region, Washington: U.S. Geological Survey Miscellaneous Investigations Series Map I-1613, 1 sheet, scale 1:250,000, with 15 p. text. [http://pubs.er.usgs.gov/publication/i1613]
- Hagen, R. A., 1987, The geology and petrology of the Northcraft Formation, Lewis County, Washington: University of Oregon Master of Science thesis, 252 p., 1 plate.
- Haugerud, R. A., 2009, Preliminary geomorphic map of the Kitsap Peninsula, Washington; version 1.0: U.S. Geological Survey Open-File Report 2009-1033, 2 sheets, scale 1:36,000. [http://pubs.usgs.gov/of/2009/1033/]
- Heiskanen, W. A.; Vening-Meinesz, F. A., 1958, The Earth and its gravity field: McGraw-Hill Book Company, Inc., 470 p.
- Hladky, F. R., 1992, Geology and mineral resources map of the Shady Cove quadrangle, Jackson County, Oregon: Oregon Department of Geology and Mineral Industries Geological Map Series GMS-52, scale 1:24,000. [https://digital.osl.state.or.us/islandora/object/osl:740]
- Hladky, F. R., 1998, Geology and mineral resources map of the Rio Canyon quadrangle, Jackson County, Oregon: Oregon Department of Geology and Mineral Industries Geological Map Series GMS-108, scale 1:24,000. [https://digital.osl.state.or.us/islandora/object/osl:791]
- Hladky, F. R.; McCaslin, G. R., 2006, Preliminary geologic map of the Springfield 7.5' quadrangle, Lane County, Oregon: Oregon Department of Geology and Mineral Industries Open File Report O-06-07. [https://digital.osl.state.or.us/islandora/object/osl:72475]
- Horwath Burnham, J. L.; Johnson, D. L., editors, 2012, Mima Mounds—The case for polygenesis and bioturbation: Geological Society of America Special Paper 490, 205 p. [https://doi.org/10.1130/SPE490]
- International Union of Geodesy and Geophysics, 1971, Geodetic Reference System 1967: International Association of Geodesy Special Publication no. 3, 116 p.
- Irvine, T. N.; Baragar, W. R. A., 1971, A guide to the chemical classification of the common volcanic rocks: *Canadian Journal of Earth Sciences*, v. 8, no. 5, p. 523–548. [https://doi.org/10.1139/e71-055]
- Koppers, A. A. P., 2002, ArArCALC—Software for  $^{40}\text{Ar}/^{39}\text{Ar}$  age calculations: *Computers and Geosciences*, vol. 28, p. 605–619. [https://doi.org/10.1016/S0098-3004(01)00095-4] (Available at <http://earthref.org/tools/ararcalc.htm>)
- Koppers, A. A. P.; Staudigel, Hubert; Wijbrans, J. R., 2000, Dating crystalline groundmass separates of altered Cretaceous seamount basalts by the  $^{40}\text{Ar}/^{39}\text{Ar}$  incremental heating technique, *Chemical Geology*, vol. 166, p. 139–158. [https://doi.org/10.1016/S0009-2541(99)00188-6]
- Koppers, A., H.; Staudigel, Hubert; Wijbrans, J. R.; Pringle, Malcolm, 2003, Short-lived and discontinuous intraplate volcanism in the South Pacific: Hot spots or extensional volcanism?: *Geochemistry, Geophysics, Geosystems*, v. 4, no. 10. [https://doi.org/10.1029/2003GC000533]
- Kuiper, K. F.; Deino, Alan; Hilgen, F. J.; Krijgsman, Wout; Renne, P. R.; Wijbrans, J. R., 2008, Synchronizing rock clocks of earth history. *Science*, v. 320, no. 5875, p. 500–504. [https://doi.org/10.1126/science.1154339]
- Lanphere, M. A.; Baadsgaard, Halfdan, 2001, Precise K–Ar,  $^{40}\text{Ar}/^{39}\text{Ar}$ , Rb–Sr and U/Pb mineral ages from the 27.5 Ma Fish Canyon Tuff reference standard: *Chemical Geology*, vol. 175, issues 3–4. [https://doi.org/10.1016/S0009-2541(00)00291-6]
- Le Bas, M. J.; Le Maitre, R. W.; Streckeisen, A. L.; Zanettin, Bruno, 1986, A chemical classification of volcanic rocks based on the total alkali-silica diagram: *Journal of Petrology*, v. 27, part 3, p. 745–750. [https://doi.org/10.1093/petrology/27.3.745]
- Lee, J. Y.; Marti, Kurt; Severinghaus, J. P.; Kawamura, Kenji; Yoo, H.-S.; Lee, J. B.; Kim, J. S., 2006, A redetermination of the isotopic abundances of atmospheric Ar: *Geochimica et Cosmochimica Acta*, v. 70, no. 17, p. 4507–4512. [https://doi.org/10.1016/j.gca.2006.06.1563]
- Lisiecki, L. E.; Raymo, M. E., 2005, A Pliocene-Pleistocene stack of 57 globally distributed benthic  $\delta^{18}\text{O}$  records: *Paleoceanography*, v. 20, no. 1, 17 p. [https://doi.org/10.1029/2004PA001071]
- Logan, Robert L.; Walsh, Timothy J., 2009, Mima Mounds formation and their implications for climate change [abstract]. In Northwest Scientific Association, The Pacific Northwest in a changing environment--Northwest Scientific Association 81st annual meeting; Program with abstracts: Northwest Scientific Association, p. 38-39. [https://www.dnr.wa.gov/publications/ger\_presentations\_nwsa\_2009\_logan.pdf]
- Logan, R. L.; Walsh, T. J.; Stanton, B. W.; Sarikhan, I. Y., 2009, Geologic map of the Maytown 7.5-minute quadrangle, Thurston County, Washington: Washington Division of Geology and Earth Resources Geologic Map GM-72, 1 sheet, scale 1:24,000. [http://www.dnr.wa.gov/Publications/ger\_gm72\_geol\_map\_maytown\_24k.pdf]
- Ludwig, K. R., 2012, Isoplot 3.75: A geochronological toolkit for Microsoft Excel: Special Publication no. 5, Berkeley Geochronological Center, Berkeley, California, 75 p.



- Madin, I. P.; Murray, R. B.; Hladky, F. R., 2006, Preliminary geologic map of the Coburg 7.5' quadrangle, Lane and Linn Counties, Oregon: Oregon Department of Geology and Mineral Industries Open File Report O-06-06. [https://digital.osl.state.or.us/islandora/object/osl:86294]
- Magsino, Sammantha; Sanger, Elizabeth; Walsh, T. J.; Palmer, S. P.; Blakely, R. J., 2003, The Olympia structure: Ramp or discontinuity? New gravity data provide more information [abstract]: Geological Society of America Abstracts with Programs, v. 35, no. 6, p. 479. [https://gsa.confex.com/gsa/2003AM/webprogram/Paper67057.html]
- McBirney, A. R., 1978, Volcanic evolution of the Cascade Range: Annual Reviews of Earth and Planetary Sciences, v. 6, p. 437–456. [https://adsabs.harvard.edu/full/1978AREPS...6..437M]
- McCaffrey, Robert; King, R. W.; Payne, S. J.; Lancaster, Matthew, 2013, Active tectonics of northwestern U. S. inferred from GPS-derived surface velocities: Journal of Geophysical Research Solid Earth, v. 118, no. 2, p. 709–723. [https://doi.org/10.1029/2012JB009473]
- Min, Kyoungwon; Mundil, Roland; Renne, P. R.; Ludwig, K. R., 2000, A test for systematic errors in  $^{40}\text{Ar}/^{39}\text{Ar}$  geochronology through comparison with U-Pb analysis of a 1.1-Ga rhyolite: Geochimica et Cosmochimica Acta, v. 64, p. 73–98. [https://doi.org/10.1016/S0016-7037(99)00204-5]
- Morelli, Carlo, editor, 1974, The International Gravity Standardization Net, 1971: International Association of Geodesy Special Publication no. 4, 194 p.
- Morrison, R. B., 1991, Introduction. In Morrison, R. B., editor, Quaternary nonglacial geology—Conterminous U.S.: Geological Society of America, Decade of North American Geology, Geology of North America, v. K-2, p. 1–12.
- Mundorff, M. J.; Weigle, J. M.; Holmberg, G. D., 1955, Ground water in the Yelm area, Thurston and Pierce Counties, Washington: U.S. Geological Survey Circular 356, 58 p., 2 plates. [http://pubs.er.usgs.gov/publication/cir356]
- Nelson, A. R.; Personius, S. F.; Sherrod, B. L.; Buck, Jason; Bradley, Lee-Ann; Henley, Gary, II; Liberty, L. M.; Kelsey, H. M.; Witter, R. C.; Koehler, R. D.; Schermer, E. R.; Nemser, E. S.; Cladouhos, T. T., 2008, Field and laboratory data from an earthquake history study of scarps in the hanging wall of the Tacoma fault, Mason and Pierce Counties, Washington: U.S. Geological Survey Scientific Investigations Map SIM-3060, 3 sheets, scale 1:30,000. [http://pubs.usgs.gov/sim/3060/]
- Noble, J. B.; Wallace, E. F., 1966, Geology and ground-water resources of Thurston County, Washington; Volume 2: Washington Division of Water Resources Water Supply Bulletin 10, v. 2, 141 p., 5 plates. [https://apps.ecology.wa.gov/publications/SummaryPages/WSB10b.html]
- Odum, J. K.; Stephenson, W. J.; Pratt, T. L.; Blakely, R. J., 2016, Shallow geophysical imaging of the Olympia anomaly: An enigmatic structure in the southern Puget Lowland, Washington State: Geosphere, v. 12, no. 5, p. 1617–1632. [https://doi.org/10.1130/GES01248.1]
- Paces, J. B.; Miller, J. D., Jr., 1993, Precise U-Pb ages of Duluth Complex and related mafic intrusions, northeastern Minnesota: Geochronological insights to physical, petrogenetic, paleomagnetic, and tectonomagmatic processes associated with the 1.1 Ga Midcontinent Rift System: Journal of Geophysical Research, v. 98, p. 13997–14013. [https://doi.org/10.1029/93JB01159]
- Parker, B. L.; Goldstein, B. S.; Futornick, Z. O.; Pringle, P. T., 2008, Sedimentological evidence for an enriched glacial outburst flood in Thurston County, Washington [abstract]: Geological Society of America Abstracts with Programs, v. 40, no. 1, p. 70.
- Paton, Chad; Hellstrom, John; Paul, Bence; Woodhead, Jon; Hergt, Janet, 2011, Iolite: Freeware for the visualisation and processing of mass spectrometric data: Journal of Analytical Atomic Spectrometry, v. 26, p. 2508–2518. [https://doi.org/10.1039/C1JA10172B]
- Peck, D. L.; Griggs, A. B.; Schlicker, H. G.; Well, F. G.; Dole, H. M., 1964, Geology of the central and northern parts of the Western Cascade Range in Oregon: U. S. Geological Survey Professional Paper 449, 56 p., 1 plate. [https://pubs.er.usgs.gov/publication/pp449]
- Phillips, W. M.; Walsh, T. J.; Hagen, R. A., 1989, Eocene transition from oceanic to arc volcanism, southwest Washington. In Muffler, L. J. P.; Weaver, C. S.; Blackwell, D. D., editors, Proceedings of workshop XLIV—Geological, geophysical, and tectonic setting of the Cascade Range: U.S. Geological Survey Open-File Report 89-178, p. 199–256. [http://pubs.er.usgs.gov/publication/ofr89178]
- Phillips, J. D.; Hansen, R. O.; Blakely, R. J., 2007, The use of curvature in potential-field interpretation: Exploration Geophysics, v. 38, p. 111–119. [https://doi.org/10.1071/EG07014]
- Pierce County, 2011, Pierce 2011 project, Pierce County Washington lidar, collected between April 23, 2011 and September 3, 2011 by Watershed Sciences Inc., 3-ft resolution, accessed June 2021 [http://lidarportal.dnr.wa.gov/], metadata available on portal [ger\_pierce\_2011\_lidar\_report.pdf].
- Plouff, Donald, 2000, Field estimates of gravity terrain corrections and Y2K-compatible method to convert from gravity readings with multiple base stations to tide-and long-term drift-corrected observations: U.S. Geological Survey Open-File Report OF-00-140, 35 pp. [https://doi.org/10.3133/ofr00140]
- Polenz, Michael; Alldritt, Katelin; Hehemann, N. J.; Sarikhan, I. Y.; Logan, R. L., 2009, Geologic map of the Belfair 7.5-minute quadrangle, Mason, Kitsap, and Pierce Counties, Washington: Washington Division of Geology and Earth Resources Open File Report 2009-7, 1 sheet, scale 1:24,000. [http://www.dnr.wa.gov/Publications/ger\_ofr2009-7\_geol\_map\_belfair\_24k.pdf]
- Polenz, Michael; Petro, G. T.; Contreras, T. A.; Stone, K. A.; Legorreta Paulín, Gabriel; Cakir, Recep, 2013, Geologic map of the Seabeck and Poulsbo 7.5-minute quadrangles, Kitsap and Jefferson Counties, Washington: Washington Division of Geology and Earth Resources Map Series 2013-02, 1 sheet, scale 1:24,000, 39 p. text. [http://www.dnr.wa.gov/Publications/ger\_ms2013-02\_geol\_map\_seabeck-poulsbo\_24k.zip]
- Polenz, Michael; Favia, J. G.; Hubert, I. J.; Legorreta Paulín, Gabriel; Cakir, Recep, 2015, Geologic map of the Port Ludlow and southern half of the Hansville 7.5-minute quadrangles, Kitsap and Jefferson Counties, Washington: Washington Division of Geology and Earth Resources Map Series 2015-02, 1 sheet, scale 1:24,000, 40 p. text. [http://www.dnr.wa.gov/publications/ger\_ms2015-02\_geol\_map\_port\_ludlow\_hansville\_24k.zip]
- Polenz, Michael; Allen, M. D.; Legorreta Paulín, Gabriel; Eungard, D. W.; Cakir, Recep; Scott, S. P.; Mahan, S. A., 2016, Geologic map of the Shelton Valley 7.5-minute quadrangle, Mason County, Washington: Washington Division of Geology and Earth Resources Map Series 2016-02, 1 sheet, scale 1:24,000, 45 p. text. [http://www.dnr.wa.gov/publications/ger\_ms2016-02\_geol\_map\_shelton\_valley\_24k.zip]
- Polenz, Michael; Ostrom, B. A.; Lau, T. R.; Sadowski, A. J.; Blanks-Bennett, A. L.; Cakir, Recep; Tepper, J. H.; Legorreta Paulín, Gabriel; Nesbitt, Elizabeth; DuFrane, S. A., 2018, Geologic map of the Violet Prairie 7.5-minute quadrangle, Thurston and Lewis Counties, Washington: Washington Geological Survey Map Series 2018-04, 1 sheet, scale 1:24,000, 41 p. text. [http://www.dnr.wa.gov/publications/ger\_ms2018-04\_geol\_map\_violet\_prairie\_24k.zip]
- Polenz, Michael; Toth, C. H.; Samson, Catherine; Sadowski, A. J.; Becerra, R. I.; Lau, T. R.; Anderson, M. L.; Nesbitt, E. A.; Tepper, J. H.; DuFrane, S. A.; Legorreta Paulín, Gabriel, 2019, Geologic map of the Rochester 7.5-minute quadrangle, Thurston and Lewis Counties, Washington: Washington Geological Survey Map Series 2019-02, 1 sheet, scale 1:24,000. [http://www.dnr.wa.gov/publications/ger\_ms2019-02\_geol\_map\_rochester\_24k.zip]

- Polenz, Michael; Samson, Catherine; Reedy, Tabor; von Dassow, Wesley; Duckworth, C. W.; Lau, T. R.; Anderson, M. L.; Nesbitt, E. A.; Tepper, J. H.; DuFrane, S. A.; Legoretta Paulín, Gabriel, 2020, Geologic map of the Oakville and Rainbow Falls 7.5-minute quadrangles, Lewis, Thurston, and Grays Harbor Counties, Washington: Washington Geological Survey Map Series 2020-02, 1 sheet, scale 1:24,000, 19 p. text. [[http://www.dnr.wa.gov/publications/ger\\_ms2020-02\\_geol\\_map\\_oakville\\_rainbow\\_falls\\_24k.zip](http://www.dnr.wa.gov/publications/ger_ms2020-02_geol_map_oakville_rainbow_falls_24k.zip)]
- Polenz, Michael; Hladky, F. R.; Anderson, M. L.; Tepper, J. H.; Horst, A. E.; Miggins, D. P.; Legoretta Paulín, Gabriel, 2021, Geologic map of the Tenalquot Prairie and northern two-thirds of the Vail 7.5-minute quadrangles, Thurston and Pierce Counties, Washington: Washington Geological Survey Map Series 2021-02, 1 sheet, scale 1:24,000, 47 p. text. [[https://www.dnr.wa.gov/publications/ger\\_ms2021-02\\_geol\\_map\\_tenalquot\\_prairie\\_northern\\_vail\\_24k.zip](https://www.dnr.wa.gov/publications/ger_ms2021-02_geol_map_tenalquot_prairie_northern_vail_24k.zip)]
- Porter, S. C.; Swanson, T. W., 1998, Radiocarbon age constraints on rates of advance and retreat of the Puget lobe of the Cordilleran ice sheet during the last glaciation: *Quaternary Research*, v. 50, no. 3, p. 205–213. [<http://courses.washington.edu/twsteach/ESS/Research/QR%2098%20205-213.pdf>]
- Pratt, T. L.; Johnson, S. Y.; Potter, C. J.; Stephenson, W. J.; Finn, C. A., 1997, Seismic reflection images beneath Puget Sound, western Washington State—The Puget Lowland thrust sheet hypothesis: *Journal of Geophysical Research*, v. 102, no. B12, p. 27469–27489. [<https://doi.org/10.1029/97JB01830>]
- Pringle, P. T., 2008, Roadside geology of Mount Rainier National Park and vicinity: Washington Division of Geology and Earth Resources Information Circular 107, 190 p. [[https://fortress.wa.gov/dnr/geologydata/Publications/ic107\\_mt\\_rainier\\_road\\_guide.pdf](https://fortress.wa.gov/dnr/geologydata/Publications/ic107_mt_rainier_road_guide.pdf)]
- Pringle, P. T.; Goldstein, B. S., 2002, Deposits, erosional features, and flow characteristics of the late-glacial Tanwax Creek–Ohop Creek Valley flood—A likely source for sediments composing the Mima Mounds, Puget Lowland, Washington [abstract]: *Geological Society of America Abstracts with Programs*, v. 34, no. 5, p. A-89.
- Sadowski, A. J.; Keller, W. E.; Polenz, Michael; Lau, T. R.; Cakir, Recep; Nesbitt, Elizabeth; Tepper, J. H.; DuFrane, S. A.; Legoretta Paulín, Gabriel, 2018, Geologic map of the Centralia 7.5-minute quadrangle, Lewis County, Washington: Washington Geological Survey Map Series 2018-05, 1 sheet, scale 1:24,000, 43 p. text. [[http://www.dnr.wa.gov/publications/ger\\_ms2018-05\\_geol\\_map\\_centralia\\_24k.zip](http://www.dnr.wa.gov/publications/ger_ms2018-05_geol_map_centralia_24k.zip)]
- Sadowski, A. J.; Becerra, R. I.; Toth, C. H.; Polenz, Michael; Anderson, M. L.; Lau, T. R.; Nesbitt, E. A.; Tepper, J. H.; DuFrane, S. A., 2019, Geologic map of the Adna 7.5-minute quadrangle, Lewis County, Washington: Washington Geological Survey Map Series 2019-01, 1 sheet, scale 1:24,000. [[http://www.dnr.wa.gov/publications/ger\\_ms2019-01\\_geol\\_map\\_adna\\_24k.zip](http://www.dnr.wa.gov/publications/ger_ms2019-01_geol_map_adna_24k.zip)]
- Schasse, H. W., compiler, 1987, Geologic map of the Centralia quadrangle, Washington: Washington Division of Geology and Earth Resources Open File Report 87-11, 28 p., 1 plate, scale 1:100,000. [[http://www.dnr.wa.gov/Publications/ger\\_ofr87-11\\_geol\\_map\\_centralia\\_100k.zip](http://www.dnr.wa.gov/Publications/ger_ofr87-11_geol_map_centralia_100k.zip)]
- Scott, K. M.; Vallance, J. W.; Pringle, P. T., 1995, Sedimentology, behavior, and hazards of debris flows at Mount Rainier, Washington: U.S. Geological Survey Professional Paper 1547, 56 p., 1 plate. [<https://doi.org/10.3133/pp1547>]
- Sherrod, B. L., 2001, Evidence for earthquake-induced subsidence about 1100 yr ago in coastal marshes of southern Puget Sound, Washington: *Geological Society of America Bulletin*, v. 113, no. 10, p. 1299–1311. [[https://doi.org/10.1130/0016-7606\(2001\)113%3C1299:EFEISA%3E2.0.CO;2](https://doi.org/10.1130/0016-7606(2001)113%3C1299:EFEISA%3E2.0.CO;2)]
- Sisson, T. W.; Vallance, J. W., 2008, Frequent eruptions of Mount Rainier over the last ~2,600 years: *Bulletin of Volcanology*, vol. 71, p. 595–618. [<https://doi.org/10.1007/s00445-008-0245-7>]
- Sisson, T. W.; Salters, V. J. M.; Larson, P. B., 2014, Petrogenesis of Mount Rainier andesite: Magma flux and geologic controls on the contrasting differentiation styles at stratovolcanoes of the southern Washington Cascades: *Geological Society of America Bulletin*, v. 101, no. 1/2, p. 122–144. [<https://doi.org/10.1130/B30852.1>]
- Sisson, T. W.; Schmitt, A. K.; Danišik, Martin; Calvert, A. T.; Pempena, Napoleon; Huang, Chun-Yuan; Shen, Chuan-Chou, 2019, Age of the dacite of Sunset Amphitheater, a voluminous Pleistocene tephra from Mount Rainier (USA), and implications for Cascade glacial stratigraphy: *Journal of Volcanology and Geothermal Research*, v. 376, p. 27–43. [<https://doi.org/10.1016/j.jvolgeores.2019.03.003>]
- Sláma, Jiří; Košler, Jan; Condon, D. J.; Crowley, J. L.; Gerdes, Axel; Hanchar, J. M.; Horstwood, M. S. A.; Morris, G. A.; Nasdala, Lutz; Norberg, Nicholas; Schaltegger, Urs; Schoene, Blair; Tubrett, M. N.; Whitehouse, M. J., 2018, Plešovice zircon—A new natural reference material for U-Pb and Hf isotopic microanalysis: *Chemical Geology*, v. 249, no. 1-2, p. 1–35. [<https://doi.org/10.1016/j.chemgeo.2007.11.005>]
- Snively, P. D., Jr.; Roberts, A. E.; Hoover, Linn, Jr.; Pease, M. H., Jr., 1951, Geology of the eastern part of the Centralia-Chehalis coal district, Lewis and Thurston Counties, Washington: U.S. Geological Survey Coal Investigations Map C8, 2 sheets, scale 1:31,680. [<http://pubs.er.usgs.gov/publication/coal8>]
- Snively, P. D., Jr.; Brown, R. D., Jr.; Roberts, A. E.; Rau, W. W., Schopf, J. M., 1958, Geology and coal resources of the Centralia-Chehalis district, Washington: U.S. Geological Survey Bulletin 1053, 159 p., 6 plates. [<https://doi.org/10.3133/b1053>]
- Stanley, W. D.; Fuis, G. S.; Mooney, W. D., 1989, Details of crustal structure in the Cascade Range and surrounding regions from seismic and magnetotelluric data. In Muffler, L. J. P.; Weaver, C. S.; Blackwell, D. D., editors, *Proceedings of workshop XLIV--Geological, geophysical and tectonic setting of the Cascade Range*: U.S. Geological Survey Open-File Report 89-178, p. 31–73. [<http://pubs.er.usgs.gov/publication/ofr89178>]
- Steiger, R. H.; Jäger, Emilie, 1977, Subcommittee on geochronology: Convention on the use of decay constant in geo- and cosmochronology: *Earth and Planetary Science Letters*, v. 36, p. 359–362. [[https://doi.org/10.1016/0012-821X\(77\)90060-7](https://doi.org/10.1016/0012-821X(77)90060-7)]
- Sun, S.; McDonough, W. F., 1989, Chemical and isotopic systematics of oceanic basalts: Implications for mantle composition and processes. In Saunders, A. D.; Norry, M. J., editors, *Magmatism in the ocean Basins*: Geological Society of London Special Publication 42, p. 313–345. [<https://doi.org/10.1144/GSL.SP.1989.042.01.19>]
- Swick, C. A., 1942, Pendulum gravity measurements and isostatic reductions: U.S. Coast and Geodetic Survey Special Publication, v. 232, 82 pp.
- Telford, W. M.; Geldart, L. P.; Sheriff, R. E.; Keys, D. A., 1976, *Applied Geophysics*: Cambridge, 860 p.
- Thurston County Geodata Center, 2011, Thurston 2011 project, Thurston County lidar, collected between June 2011 and July 2011 by Fugro EarthData Inc, 3-ft resolution, accessed June 2020 [<http://lidarportal.dnr.wa.gov/>], metadata available on portal [[http://ger\\_thurston\\_2011\\_lidar\\_report.pdf](http://ger_thurston_2011_lidar_report.pdf)].
- Troost, K. G., 2016, Chronology, lithology and paleoenvironmental interpretations of the penultimate ice-sheet advance into the Puget Lowland, Washington State: University of Washington Doctor of Philosophy thesis, 239 p. [<https://digital.lib.washington.edu/researchworks/handle/1773/38517>]
- Troost, K. G.; Booth, D. B., 2008, Geology of Seattle and the Seattle area, Washington. In Baum, R. L.; Godt, J. W.; Highland, L. M., editors, *Landslides and engineering geology of the Seattle, Washington, area*: Geological Society of America Reviews in Engineering Geology XX, p. 1–35. [[http://www.wou.edu/las/physci/taylor/g473/seismic\\_hazards/troost\\_booth\\_2008\\_geo\\_seattle.pdf](http://www.wou.edu/las/physci/taylor/g473/seismic_hazards/troost_booth_2008_geo_seattle.pdf)]

- U.S. Geological Survey, 2016, SWWA foothills 2017 project, Western Washington 3DEP lidar, collected between Mar. 17 and Sept. 30, 2016 by Quantum Spatial Inc., 3-ft resolution, accessed June 2020 [<http://lidarportal.dnr.wa.gov/>], metadata available on portal [ger\_swwa\_foothills\_2017\_lidar\_report.pdf].
- U.S. Geological Survey Geologic Names Committee, 2018, Divisions of geologic time—Major chronostratigraphic and geochronologic units: U.S. Geological Survey Fact Sheet 2018-3054, 2 p. [<https://pubs.usgs.gov/fs/2018/3054/fs20183054.pdf>]
- Van Wagoner, T. M.; Crosson, R. S.; Creager, K. C.; Medema, G. F.; Preston, L. A.; Symons, N. P.; Brocher, T. M., 2002, Crustal structure and relocated earthquakes in the Puget Lowland, Washington, from high-resolution seismic tomography: *Journal of Geophysical Research*, v. 107, no. B12. [<https://doi.org/10.1029/2001JB000710>]
- Vermeech, Pieter, 2018, IsoPlotR: a free and open toolbox for geochronology: *Geoscience Frontiers*, v. 9, p. 1479–1493. [<https://doi.org/10.1016/j.gsf.2018.04.001>]
- Walker, J. D.; Geissman, J. W., compilers, 2009, Geologic time scale: Geological Society of America, 1 p. [<https://www.geosociety.org/documents/gsa/timescale/timescl-2009.pdf>]
- Walsh, T. J.; Logan, R. L., 2005, Geologic map of the East Olympia 7.5-minute quadrangle, Thurston County, Washington: Washington Division of Geology and Earth Resources Geologic Map GM-56, 1 sheet, scale 1:24,000. [[http://www.dnr.wa.gov/Publications/ger\\_gm56\\_geol\\_map\\_eastolympia\\_24k.pdf](http://www.dnr.wa.gov/Publications/ger_gm56_geol_map_eastolympia_24k.pdf)]
- Walsh, T. J.; Korosec, M. A.; Phillips, W. M.; Logan, R. L.; Schasse, H. W., 1987, Geologic map of Washington—Southwest quadrant: Washington Division of Geology and Earth Resources Geologic Map GM-34, 2 sheets, scale 1:250,000, with 28 p. text. [[http://www.dnr.wa.gov/publications/ger\\_gm34\\_geol\\_map\\_sw\\_wa\\_250k.pdf](http://www.dnr.wa.gov/publications/ger_gm34_geol_map_sw_wa_250k.pdf)]
- Walsh, T. J.; Logan, R. L.; Polenz, Michael; Schasse, H. W., 2003, Geologic map of the Nisqually 7.5-minute quadrangle, Thurston and Pierce Counties, Washington: Washington Division of Geology and Earth Resources Open File Report 2003-10, 1 sheet, scale 1:24,000. [[https://www.dnr.wa.gov/publications/ger\\_ofr2003-10\\_geol\\_map\\_nisqually\\_24k.pdf](https://www.dnr.wa.gov/publications/ger_ofr2003-10_geol_map_nisqually_24k.pdf)]
- Walters, K. L.; Kimmel, G. E., 1968, Ground-water occurrence and stratigraphy of unconsolidated deposits, central Pierce County, Washington: Washington Department of Water Resources Water Supply Bulletin 22, 428 p., 3 plates. [<https://fortress.wa.gov/ecy/publications/SummaryPages/WSB22.html>]
- Washburn, A. L., 1988, Mima mounds—An evaluation of proposed origins with special reference to the Puget Lowlands: Washington Division of Geology and Earth Resources Report of Investigations 29, 53 p. [[http://www.dnr.wa.gov/publications/ger\\_ri29\\_mima\\_mounds.pdf](http://www.dnr.wa.gov/publications/ger_ri29_mima_mounds.pdf)]
- Wells, R. E.; McCaffrey, Robert, 2013, Steady rotation of the Cascade arc: *Geology*, v. 41, no. 9, p. 1027–1030. [<https://doi.org/10.1130/G34514.1>]
- Wells, Ray; Bukry, David; Friedman, Richard; Pyle, Doug; Duncan, Robert; Haeussler, Peter; Wooden, Joe, 2014, Geologic history of Siletzia, a large igneous province in the Oregon and Washington Coast Range: Correlation to the geomagnetic polarity time scale and implications for a long-lived Yellowstone hotspot: *Geosphere*, v. 10, no. 4, p. 692–719. [<https://doi.org/10.1130/GES01018.1>]
- Wiedenbeck, Michael; Allé, P.; Corfu, Fernando; Griffin, W. L.; Meier, Martin; Oberli, Felix; Von Quadt, Albrecht; Roddick, J. C.; Spiegel, W., 1995, Three natural zircon standards for U-Th-Pb, Lu-Hf, trace element and REE analyses: *Geostandards Newsletters*, v. 19, p. 1–23. [<https://doi.org/10.1111/j.1751-908X.1995.tb00147.x>]
- Wiley, T. J.; Hladky, F. R., 1991, Geology and mineral resources map of the Boswell Mountain quadrangle, Jackson County, Oregon: Oregon Department of Geology and Mineral Industries Geological Map Series GMS-70, scale 1:24,000. [<https://digital.osl.state.or.us/islandora/object/osl:758>]
- Williams, I. S., 1997, U-Th-Pb geochronology by ion microprobe. In McKibben, M. A.; Shanks III, W. C.; Ridley, W. I., editors, *Applications of microanalytical techniques to understanding mineralizing processes: Reviews in Economic Geology*, v. 7, p. 1–35. [<https://doi.org/10.5382/Rev.07>]



---

## Appendix A. New Luminescence Age Estimates

### OVERVIEW

Infrared-stimulated luminescence dating estimates the time that has passed since sandy (or silty) sediment was deposited. Following sediment deposition, environmental irradiation causes electrons in feldspar grains to jump into a metastable, higher-energy spin cycle. The technique assumes that this occurs at a constant rate, such that older sediment contains proportionately more electrons in elevated spin cycles. The technique functions by measuring how much light electrons emit when released from their elevated spin cycle. This is done by subjecting the sample to infrared light that knocks the electrons out of their metastable spin cycle; their return to a lower-energy spin cycle emits light. The amount of light emitted is proportional to the time since deposition of the sample—meaning that more light is indicative of an older sample.

We use luminescence dating to constrain the depositional age of unlithified, pre-Vashon sediment exposed along the sidewalls of the Nisqually River valley, some of which previous investigators speculated may be Miocene Mashel Formation (Walters and Kimmel, 1968).

### SAMPLE COLLECTION AND PREPARATION

Samples for luminescence dating need to be collected from sediment that has not been exposed to light since its time of deposition, so the samples need to be recovered without being exposed to light. To do this, we first remove at least 2–5 cm of sand from an exposure and then pound a 4-cm diameter, 30-cm-long steel tube into the in-place sand. The lab then analyzes sand in the core of the tube, which has not been exposed to light since deposition. Additional sand from the same exposure may be exposed to light and is zip-lock-bagged for dose rate assessment, and a small vial is sealed air-tight to document field moisture content. The lab uses these supplementary samples for calibration.

### ANALYTICAL METHODS

Our samples were analyzed by the luminescence lab at the Illinois State Geological Survey, and a detailed report on their methods is in the Data Supplement.

### RESULTS

We collected and analyzed two sand samples from alluvium exposed along the sidewalls of the Nisqually River valley. Summary data are in Tables 2 and A1; full analytical data are in the Data Supplement.

**Table A1.** Optically Stimulated Luminescence (OSL) and Infrared Stimulated Luminescence results from age site GD3.

<b>Site ID</b>	GD1	<p>Compact sand 1 m above base of 44 m high cliff that forms an active, channel-right cutbank along the Nisqually River (RM28.34R). The section appears to be ancestral Nisqually River alluvium—at least 30 m of interbedded pebble gravel, sand, and lahar-deposited diamicton and bouldery gravel, directly overlain by 5 m of lahar-deposited diamicton (that yielded clast samples GD5–GD7), beneath 6–8 m of Vashon Drift.</p> <p>We sampled 30 cm below the top of a thinly planar-bedded, parallel-bedded sand (at least 1.3 m thick) at base. Gently wavy beds may locally include cross-bedding. The sand appears to gently dip west. Petrography of age sample GD1 revealed angular to rounded, poorly sorted, fine to coarse sand in which particle abundance includes devitrified glass and lithic fragment abundance &gt; quartz &gt; plagioclase &gt; ortho(?) -pyroxene &gt; opaque particles.</p> <p>Sampled Sept. 9, 2021, by Michael Polenz and Alexander Steely.</p> <p>Analysis by Sebastien Huot, Illinois Geological Survey.</p> <p>Age based on K-feldspar, central age model, corrected for anomalous fading.</p>
<b>Field sample ID</b>	MLm065c	
<b>Lab ID</b>	799	
<b>Map unit</b>	Qpc	
<b>TRS location</b>	Sec. 12, T17N R1E	
<b>Latitude (degrees)</b>	46.97603	
<b>Longitude (degrees)</b>	-122.61239	
<b>Elevation (ft)</b>	150	
Age (ka) $\pm 2\sigma$		142.6 $\pm 38.2$

<b>Site ID</b>	GD2	<p>Compact sand at base of 55 m high cliff that forms an active channel-right cutbank along the Nisqually River (RM17.1R) in Harts Lake quadrangle, 0.43 km east of map area. At the base of the cliff is ~9–11 m of mostly pebble gravel, with ~1.5 m of horizontally bedded sand at top and ~1.2 m of partly submerged, thinly- to medium-bedded, olive brown sand at base. Observed clast lithologies throughout the exposed section are consistent with Cascade Range provenance. A wavy erosional contact separates this fluvial package from 3 m of upsection pebble gravel. The section extends north into the map area and locally appears to dip north 0–2° more steeply than the active channel.</p> <p>We sampled the (moist) basal sand ~0.6 m above river water, ~0.3 m below pebble gravel. Sand beds appear parallel (no cross beds observed), gently wavy, and approximately horizontal. Petrographic review revealed well sorted, angular sand, grain size 0.2–0.5 mm, with 32% volcanic lithics, 31% plagioclase, 9% biotite, 9% pyroxene, 6% quartz, 6% opaque particles, 3% adularia (K-feldspar), and 3% red iron oxides.</p> <p>Sample is same as GD3.</p> <p>Sampled Sept. 9, 2021, by Michael Polenz and Alexander Steely.</p> <p>Analysis by Sebastien Huot, Illinois Geological Survey.</p> <p>Age based on K-feldspar, central age model, corrected for anomalous fading.</p>
<b>Field sample ID</b>	MLm047b	
<b>Lab ID</b>	798	
<b>Map unit</b>	Qpc	
<b>TRS location</b>	Sec. 1, T16N R2E	
<b>Latitude (degrees)</b>	46.90544	
<b>Longitude (degrees)</b>	-122.49446	
<b>Elevation (ft)</b>	330	
Age (ka) $\pm 2\sigma$		187.0 $\pm 58.6$

## Appendix B. New Detrital U/Pb Age Estimate

### OVERVIEW

U/Pb dating uses radioactive decay of uranium (multiple isotopes) to lead (also multiple isotopes) to estimate the crystallization age of uranium-bearing minerals. We sample rocks or sediment to assess the crystallization ages of zircons within the deposit, and thereby estimate the igneous rock crystallization age, or constrain the maximum possible age of sediment deposition. This assumes that the sediment deposit must be younger than the zircons within it. More than 100 zircons are usually analyzed from one sample of sediment or sedimentary rock. Each zircon yields a separate, individual crystal age. Because zircons of different ages within a detrital sample can have different geologic (and geographic) sources, inferences on sedimentary provenance can also be made from zircon age spectra.

### SAMPLE COLLECTION AND PREPARATION

We generally collect about 2–10 kg of freshly exposed rock per sample, while avoiding contact with soil or other surface deposits that could introduce anomalous extraneous zircons; weathering and alteration do not usually affect the age of zircon and therefore pose no concern for this technique. We send our samples to ZirChron, LLC, for mineral separation using the following procedure: Samples are pressure washed with water and then disaggregated using an Electro Pulse Disaggregator (EPD, Marx generator) at 1 Hz with discharges of ~250 kV for 15 minutes. Any clasts >500  $\mu\text{m}$  are crushed in a crusher or pulverizer. Using stainless steel sieves, the fraction between 350  $\mu\text{m}$  and 25  $\mu\text{m}$  is retained and then processed using the Wilfley water table, Frantz paramagnetic separator, and a two-step (3.00 g/cm<sup>3</sup> and 3.32 g/cm<sup>3</sup>) heavy liquid methylene iodide separation. Zircon grains from each sample are hand selected and mounted in epoxy, polished to expose the grain centers, and regions suitable for analysis are identified from optical imaging.

### ANALYTICAL METHODS

The following text is reproduced from a technical write-up by the Washington State University Radiogenic Isotope and Geochronology Laboratory with minimal modification: Zircon U-Pb ages are measured at the Radiogenic Isotope and Geochronology Lab (RIGL) at Washington State University using an Analyte G2 193 excimer laser ablation system coupled with a Thermo-Finnigan Element 2 single-collector inductively coupled plasma mass spectrometer. The laser parameters are 25- $\mu\text{m}$ -diameter spot size, 10 Hz repetition rate, and fluence of ~5.0 J/cm<sup>2</sup>. For the U-Pb measurement, we mostly followed the method of Chang and others (2006), except for the use of a 193-nm laser system. A 10-second blank measurement of the He and Ar carrier gasses (laser off) before each analysis is followed by 250 scans across masses <sup>202</sup>Hg, <sup>204</sup>Pb+Hg, <sup>206</sup>Pb, <sup>207</sup>Pb, <sup>208</sup>Pb, <sup>232</sup>Th, <sup>235</sup>U, and <sup>238</sup>U during ~30-second laser ablation period. Analyses of zircon unknowns, standards and quality control zircon grains are interspersed with analyses of external calibration standards, typically with 10–12 unknowns bracketed by multiple analyses of two different zircon standards (Plešovice and FC-1). The Plešovice standard (337 Ma; Sláma and others, 2008) is used to calibrate the <sup>206</sup>Pb/<sup>238</sup>U and <sup>207</sup>Pb/<sup>235</sup>U ages, and the FC-1 standard (1,099 Ma; Paces and Miller, 1993) is used for calibration of <sup>207</sup>Pb/<sup>206</sup>Pb ages owing to its high count rate for <sup>207</sup>Pb (~2–4 times higher than that of Plešovice). Zircon 91500 (1,065 Ma; Wiedenbeck and others, 1995), Fish Canyon Tuff (~27.5 Ma; Lanphere and others, 2001) and Temora2 (417 Ma; Black and others, 2004) are used as quality control standards. Data are processed offline using the Iolite software (Paton and others, 2011). Common Pb correction is performed using the <sup>207</sup>Pb method (Williams, 1997).

### RESULTS

We collected and analyzed two samples; one is sandy matrix from conglomerate (or diamictite) north of the Deschutes River, the other is a sand bed in alluvium exposed along the eastern sidewall of the Nisqually River valley. Both sites had been previously mapped as possible (Miocene) Mashel Formation (Noble and Wallace, 1966; Walters and Kimmel, 1968). Isochron ages, weighted-mean ages, concordia ages, and discordance filters (-5% to +15%) are made using IsoPlotR (Vermeesch, 2018). Reported ages are weighted means computed by Michael Polenz 3/22/2022; errors exclude overdispersion. Summary data are in Tables 2 and B1; individual zircon ages and analytical data are in the Data Supplement.



**Table B1.** Detrital zircon maximum constraining ages from age sites GD3 and GD4. See Data Supplement for full analytical results.

Site ID	GD3	<p>Compact sand at base of 55-m-high cliff that forms an active, channel-right cutbank along the Nisqually River (RM17.1R) in Harts Lake quadrangle, 0.43 km east of map area. At base of cliff is ~9–11 m of mostly pebble gravel, with ~1.2 m of partly submerged, thinly- to medium-bedded, olive brown sand at base. Sand beds appear parallel (no cross beds observed), gently wavy, and approximately horizontal. Petrographic review revealed well-sorted, angular sand, grain size 0.2–0.5 mm, with 32% volcanic lithics, 31% plagioclase, 9% biotite, 9% pyroxene, 6% quartz, 6% opaque particles, 3% adularia (K-feldspar), and 3% red iron oxides. Observed clast lithologies throughout the exposed section are consistent with Cascade Range provenance. The section extends north into the map area and locally appears to dip north 0–2° more steeply than the active channel.</p> <p>We sampled the basal sand ~0.6 m above river water, ~0.3 m below pebble gravel. Sample is same as GD2. Sampled Sept. 9, 2021, by Michael Polenz and Alex Steely.</p> <p>Reported age is weighted mean of 60 ages at the young end of the spectrum. Youngest age excluded as outlier with large error; older ages excluded because they form a clear trend away from the young cluster.</p> <p>2σ error with overdispersion = 0.0214 Ma (n=60/116); MSWD = 5.10</p>
Field sample ID	MLm047b	
Map unit	Qpc	
TRS location	Sec. 1, T16N R2E	
Latitude (degrees)	46.90544	
Longitude (degrees)	-122.49446	
Elevation (ft)	330	
Age (Ma) ±2σ		1.0189 ±0.0093

Site ID	GD4	<p>Sandy matrix from conglomerate. Petrographic review reveals immature, poorly sorted volcanic lithic sandstone (arenite) with very angular to subrounded grains 0.1–2 mm in diameter. Particles include: 50–60% subrounded pilotaxitic andesite lithics, 1–2 mm; 10–20% subrounded to sub-angular trachytic andesite lithics, 0.5–1 mm; 5–10% individual subangular plagioclase crystals, 0.3–1 mm; 5–7% subrounded to angular devitrified glass, 0.2–1 mm; 5–7% subrounded intersertal andesite lithics, 0.5–1 mm; traces to 1% very angular to subrounded quartz, 0.2–0.5 mm.</p> <p>Sampled Aug 30, 2021, by Michael Polenz and Maria Furtney.</p> <p>Reported age is weighted mean of 69 ages that form a distinctive cluster at the young end of the spectrum. Older ages excluded because all are older than the Cascade Range and Northcraft Fm.</p> <p>2σ error with overdispersion = 0.183 Ma (n=69/131) MSWD = 6.30</p>
Field sample ID	MLm110	
Map unit	Evcn	
TRS location	Sec. 34, T16N R2E	
Latitude (degrees)	46.834658	
Longitude (degrees)	-122.53845	
Elevation (ft)	490	
Age (Ma) ±2σ		36.952 ± 0.072

## Appendix C. New $^{40}\text{Ar}/^{39}\text{Ar}$ Age Estimates

### OVERVIEW

Argon dating uses the radioactive decay of  $^{40}\text{K}$  to  $^{40}\text{Ar}$  to determine the age of potassium-bearing minerals and materials. We use argon dating to estimate the crystallization ages of Northcraft Formation dacite and andesite lavas, and clasts in Northcraft Formation lahar deposits. We also use this dating method to estimate the crystallization ages of clasts in Quaternary lahar deposits exposed along the sidewalls of the Nisqually River valley, in hopes of establishing a maximum constraining age for the lahars.

### SAMPLE COLLECTION AND PREPARATION

Samples for argon dating are collected from in-place volcanic or volcanoclastic rock and should have as little weathering and alteration as possible. We prioritize relatively unweathered rock with few fractures, though such exposures are not abundant in the map area. Blocks of the outcrop are broken into smaller pieces to remove weathering rinds. We then place about 1–3 kg of rock into a bag. Candidate sample sites are ranked based on many factors, including the desire for spatial coverage, stratigraphic location, rock type, and budgetary constraints. Of those samples that will be analyzed, we select the freshest pieces and send 1–2 kg of material to the lab for irradiation and analysis.

### ANALYTICAL METHODS

The following section of text is reproduced from an analytical report provided by the Oregon State University Argon Geochronology Laboratory, with minimal modification:

Samples were crushed, sieved, washed, and dried using standard mineral separation techniques. Groundmass splits were obtained for the sample, rinsed with cold water, then dried in a drying oven at 55 °C. Once the samples were dried, they were sieved to 250–150  $\mu\text{m}$ . Special care was taken to remove any alteration material by using an intensive acid leaching procedure using a combination of HCl and HNO<sub>3</sub> at different acid strength (Koppers and others, 2000). A final separate of groundmass was obtained using a binocular microscope. Any visible alteration or adhering crystal phases were carefully removed prior to packaging and irradiation of the sample.

$^{40}\text{Ar}/^{39}\text{Ar}$  ages were obtained by incremental heating methods using the ThermoFisher Scientific ARGUS-VI mass spectrometer and data collection using internal lab software ArArExperiments version 4.4.0. The samples were irradiated for 6 hours. Samples were irradiated with the Fish Canyon Tuff sanidine (FCT-2-NM sanidine) with an age of  $28.201 \pm 0.023$  Ma,  $1\sigma$  flux monitor (Kuiper and others, 2008). Individual J-values for each sample were calculated by polynomial extrapolation of the measured flux gradient against irradiation height and typically give 0.06–0.12 percent uncertainties ( $1\sigma$ ). The  $^{40}\text{Ar}/^{39}\text{Ar}$  incremental heating age determinations were performed on a multi-collector ARGUS-VI mass spectrometer at Oregon State University that has 5 Faraday collectors fitted to two 1,012 ohm resistors for masses  $^{41}\text{Ar}$  and  $^{40}\text{Ar}$  and three 1,013 ohm resistors for argon masses  $^{39}\text{Ar}$ ,  $^{38}\text{Ar}$ , and  $^{37}\text{Ar}$  and 1 ion-counting CuBe electron multiplier (located in a position next to the lowest mass Faraday collector). This allows us to measure simultaneously all argon isotopes, with mass 36 on the multiplier and masses 37 through 40 on the four adjacent Faradays. This configuration provides the advantages of running in a full multi-collector mode while measuring the lowest peak (on mass 36) on the highly sensitive electron multiplier (which has an extremely low dark-noise and a very high peak/noise ratio). Irradiated samples were loaded into Cu-planchettes in an ultra-high vacuum sample chamber and incrementally heated by scanning a Synrad Firestar 20-watt defocused CO<sub>2</sub> laser beam in pre-set patterns across the sample, in order to release the argon evenly. Each heating step is 62 seconds. After heating, reactive gasses were cleaned up using four SAES Zr-Al AP10 getters for 3 minutes; two operated at 450°C and two operated at room temperature (21°C). All ages were calculated using the corrected Steiger and Jäger (1977) decay constant of  $5.530 \pm 0.097 \times 10^{-10} \text{ yr}^{-1}$  ( $2\sigma$ ) as reported by Min and others (2000). For all other constants used in the age calculations we refer to table 2 in Koppers and others (2003). Incremental heating plateau ages and isochron ages were calculated as weighted means with  $1/\sigma^2$  as weighting factor and as YORK2 least-square fits with correlated errors using the ArArCALC v2.6.2 software from Koppers (2002) available at <http://earthref.org/ArArCALC/>.

Argon isotopic results are corrected for system blanks, radioactive decay, mass discrimination, reactor-induced interference reactions, and atmospheric argon contamination. Decay constants reported by Min and others (2000) are utilized for age calculation. Isotope interference corrections as determined using the ARGUS VI are:  $(^{36}\text{Ar}/^{37}\text{Ar})\text{Ca} = 0.0002703 \pm 0.000005$ ;  $(^{39}\text{Ar}/^{37}\text{Ar})\text{Ca} = 0.0006425 \pm 0.0000059$ ;  $(^{40}\text{Ar}/^{39}\text{Ar})\text{K} = 0.000607 \pm 0.000059$ ;  $(^{38}\text{Ar}/^{39}\text{Ar})\text{K} = 0.012077 \pm 0.000011$ . Ages were calculated assuming an atmospheric  $^{40}\text{Ar}/^{36}\text{Ar}$  ratio of  $298.56 \pm 0.113$  (Lee and others, 2006). Data reduction and age calculation were processed using  $^{40}\text{Ar}/^{39}\text{Ar}$  Calc 2.7.0 (Koppers, 2002). Plateau ages are defined as including >50% of the total  $^{39}\text{Ar}$  released with at least three consecutive steps, where the  $^{40}\text{Ar}/^{39}\text{Ar}$  ratio for each step is in agreement with the mean at the 95% confidence level. In many cases only a mini-plateau age is given, where a mini-plateau is <50% of the  $^{39}\text{Ar}$  released.















## Appendix D. Gravity and Magnetic Data

### GRAVITY

#### Overview and purpose

Lateral changes in isostatic gravity across a region result from density changes within rocks of the mid- to- upper crust. Gravity surveys are especially useful in delineating steeply dipping contacts between two rock bodies that have a large contrast in density. Areas of high gravity indicate that high-density rocks (for example many igneous and metamorphic rocks) are closer to the surface. Areas of low gravity indicate less-dense material near the surface, for instance, low-density sediment in sedimentary basins. Gridding gravity measurements creates a map that outlines areas of high gravity and low gravity. Gravity data, paired with other measurable geophysical constraints, allow us to create models of the subsurface that quantitatively predict observed data. When combined with surficial geologic information and density measurements of surficial rocks, gravity can become a powerful modeling tool.

The goals of this gravity survey are to: (1) delineate density contrasts within the subsurface, (2) determine length and geometry of known structures, (3) identify previously unknown structures, and (4) provide geophysical constraints to be used in our forward modeling of the subsurface which may constrain the geometry of subsurface density contrasts.

#### Description of Method

##### FIELD METHODS AND SAMPLED LOCATIONS

Data collected with a Lacoste & Romberg G gravimeter (serial # G-908) and Scintrex CG-6 meter (Serial # 19050174), supplement older datasets compiled by Finn and others (1991) and PACES (now defunct; data obtained from B. Drenth, U.S. Geological Survey, written communication, 2020). We utilized the gravity base station 'OLYK' to tie our data to the U.S. gravity network. Gravity station spacing at roughly 2 km generates a basic grid over a large area. In areas where known structures exist or initial gravity data collection showed a significant gradient, station spacing is 1 km to provide greater resolution. For modeled cross section lines, station spacing is roughly 250 m along the line, as access warrants. Selecting sites that avoid great topographical relief as much as possible reduces field terrain corrections. Sites with minimal tree cover maximize the effectiveness of the GPS unit (Javad Triumph-2). When tree cover is unavoidable, lengthening the recording time of the GPS unit accordingly provides the best possible vertical accuracy in elevation measurements. Where available, measurements made on exposed bedrock provide ground-truth for map interpretation and modeling. Bedrock density samples and magnetic susceptibility measurements of outcrops constrain geophysical modeling as much as possible at these locations.

##### DATA REDUCTION AND PROCESSING

A Javad Triumph-2 differential GPS unit provided the horizontal and vertical position of each station. The proprietary Javad Justin software allows for careful data editing and post-processing for differential correction utilizing the National Oceanic and Atmospheric Administration and the National Geodetic Survey's Continuously Operating Reference Stations (CORS) within 70 km of the study area. After processing, typical positional accuracy is 0.15 m in the vertical and horizontal. Lidar elevation replaces GPS elevation where GPS elevation is suspect and lidar data appears to be good. We apply the factory instrument (gravimeter) calibration constants to each gravity observation, augmented by correction factors obtained from the Mount Hamilton calibration loop east of San Jose, CA (Barnes and others, 1969), and correcting for Earth tides to produce observed gravity values. The data reference the International Gravity Standardization Net of 1971 (Morelli, 1974) and the reference ellipsoid is the Geodetic Reference System of 1967 (International Union of Geodesy and Geophysics, 1971). The assumed linear drift between base-station ties results in a maximum gravity reading error of 0.05 mGal.

Gravity data reduction formulas for the free-air anomaly are standard (for example, Telford and others, 1976; Swick, 1942) and applying Bouguer, and terrain corrections out to 166.7 km from each station produces a complete Bouguer anomaly. Earth curvature corrections were not applied to this data. Terrain corrections are a combination of a field-based component (to a radius of 68 m using the Hayford system; Plouff, 2000) and a computer-generated component (using 30-m USGS DEM digital grids). To assist in the interpretation of mid- to upper-crustal density contrasts, the complete Bouguer anomaly is further reduced to an isostatic anomaly by applying formulas that adjust for long-wavelength variations, such as those caused by the existence of a crustal root and (or) upper-mantle density contrasts. An Airy-Heiskanen model (Heiskanen and Vening-Meinesz, 1958) produces the isostatic correction, assuming a 25-km-thick crust at sea level and a crust-mantle density contrast of 400 kg/m<sup>3</sup>. All parts of the data-reduction process assume a standard reduction density of 2,670 kg/m<sup>3</sup>. Gravity readings and computed anomalies are in the Data Supplement.

Uncertainties in the gravity data are predominantly due to uncertainty in vertical position and the terrain corrections. Elevation data in this study have average uncertainties of 0.19 m (but range to a maximum of 2.6 m). Thus the vertical position uncertainty results in an average gravity data uncertainty of 0.04 mGal, up to a maximum of 0.52 mGal for a few data points. The uncertainty associated with terrain corrections is generally only 5–10 percent of the actual correction. This results in an average terrain-correction uncertainty of 0.08–0.15 mGal but varies according to topography. Average uncertainty in steep and hilly regions

is 0.12–0.23 mGal, whereas average uncertainty in flatter areas is 0.05–0.1 mGal. Based on this, gravity anomalies of 0.6–1 mGal and greater reflect interpretable density variations in the upper crust.

The minimum-curvature algorithms in the GIS software package Geosoft Oasis Montaj transform our point isostatic anomaly data into gridded surfaces. The maximum horizontal gradients (referred to as “max-spots”) calculated using the curvature analysis methodology of Phillips and others (2007) quantitatively locate strong and linear boundaries between rocks in the subsurface that have substantial density differences.

## **GEOMAGNETICS**

### **Overview and Purpose**

Magnetic surveys map the changes in the earth’s magnetic field due to local magnetic sources at high resolution. This method delineates contacts between geologic units of contrasting magnetic properties, particularly in the mid to upper crust. A large number of magnetic profiles help to precisely determine magnetic contacts and trace them across a map area. Individual profiles, coupled with magnetic susceptibility measurements of surficial rocks, are powerful geophysical constraints for 2D subsurface modeling.

### **Description of Method**

Aeromagnetic data used in this study were acquired in 1995 and 2016 (Blakely and others, 1999, 2020) via low-flying aircraft with a stinger-mounted magnetometer. For the 1995 survey, north–south flight lines are 0.4 km apart, with east–west tie lines spaced at 8 km. For the 2016 survey, east–west flight lines are 0.4 km apart and north–south tie lines at 4 km. Aeromagnetic measurements were interpolated to a projected, rectilinear grid using a bi-directional gridding algorithm within the GIS software package Geosoft Oasis Montaj. Another filter reduces this anomaly to the magnetic pole, more closely centering anomalies over their sources for map-view interpretation. We apply a filter to the aeromagnetic map to enhance short-wavelength anomalies from shallower sources (termed ‘residual’). The residual results from subtracting a version of the original aeromagnetic grid that has been filtered (upward continued 50 m to enhance long-wavelength anomalies) from the original grid. The residual retains short-wavelength anomalies that mainly reflect the effects from sources in the upper couple kilometers of the crust. This method does not produce anomalies reflecting a precise depth of sources, but can separate out anomalies sourced generally deeper or shallower. The same algorithm used to determine the gravity max-spots is applied to residual grids to quantitatively locate strong and linear gradients (lineaments) that correspond to sharp and linear subsurface geologic boundaries.

## **HAND-SAMPLE PROPERTIES**

We collected bedrock samples throughout the study area for laboratory analysis. We weighed samples using an A & D company limited FX-3000i WP analytical balance. Three measurements per sample combine to determine density: a dry weight in air, a submerged (water-saturated) weight, and a water-saturated weight in air. While these measurements produce grain density, saturated bulk density, and dry bulk density, saturated bulk density best reflects subsurface conditions and was therefore referenced for modeling. Magnetic susceptibility measurements taken with a KT10 Kappa Meter accompany rock sample density measurements, and we use the same meter to collect direct readings from outcrops where possible. Weathering tends to replace denser minerals with less dense weathering products and turn magnetite into less magnetic minerals like hematite. Therefore, all of our measured rock densities and susceptibilities from surface outcrops (see Data Supplement) can be considered minimum values.

## **QUANTITATIVE CROSS-SECTION MODELING**

### **Overview and Purpose**

Quantitative 2-D forward modeling of cross sections constrained by potential-field data provides insight into subsurface unit and fault geometry that go beyond qualitative interpretations of map-view data. This technique helps provide the best possible interpretation of fault type (for example normal, reverse, or strike-slip), fault dip in the upper crust (for example steep or shallow), and offset across the fault on units with particularly strong physical-property contrasts with surrounding rocks. This method also can identify blind faults that have little surface expression and are difficult to capture via surface geology observations.

### **Description of Method**

GM-SYS provides the platform for computing the sum effect of blocks of rock in the subsurface in a 2-D cross section on both the gravitational and geomagnetic fields of the Earth. This is a forward-modeling method. This means the operator hypothesizes which rock types are in the subsurface, their location, and their volume, and the GM-SYS program predicts the total fields that result from that particular model. The operator’s responsibility is to refine the hypothesis until the predicted potential-fields match the data measured in the field. This ensures that any cross-section interpretation of the subsurface matches two additional data types



(for example gravity and magnetism) besides the geology, and thus reduces the number of potential hypotheses for the subsurface geometry of rocks.

Several types of data constrain this process in addition to the gravity and aeromagnetic data. Surface geologic observations define rocks that are in the model's near-surface topography and lab measurements (see above) of density and magnetic properties of hand samples gathered from the surface provide additional rock property constraints. Also essential is the knowledge of the operator and collaborators in the project about the geologic history, expected stratigraphy in the subsurface, and structural geometries that are physically possible based on standard geologic mapping and cross-section construction techniques.

Within these constraints, there is still the strong possibility that multiple hypotheses of subsurface geometry can fit the gravity and magnetic data within the accepted error for those two data types. Therefore, care in the construction of models helps define which parts of the subsurface model are well-constrained with the fewest alternative hypotheses and which parts could have multiple possible geometries. In general, potential-field data provide strong constraint (including their position and dip) on simple, steeply-dipping boundaries that juxtapose rocks with strong differences in physical properties. Potential-field data provide very poor constraint on horizontal boundaries or boundaries between rocks with little contrast in physical properties. Depth of sub-horizontal stratigraphic boundaries within sedimentary rocks is particularly suspect and is never well-constrained without the addition of good quality well or reflection-seismic data. Depth of sub-horizontal boundaries between units of strongly contrasting properties is resolvable but dependent on uncertainties in the physical properties of those units. In those cases, depth of a boundary can trade off with density or magnetism of the rocks.

Our approach first constructs initial simplified models, including uniform packages of sediment, sedimentary rock, metamorphic rock, or volcanic rock to fit the overall long-wavelength features in the gravity and magnetic data. Our model space extends beyond the end of the models shown in this report to avoid edge effects due to truncated subsurface volumes. Adding detail in the stratigraphy and decreasing the size of blocks after the major fit allows modeling of smaller-scale features that fit shorter wavelength anomalies, particularly near the surface. During each iteration, we test possible options for physical properties of rocks and geometries of boundaries permitted by the surface geology observations and measured rock-property constraints. Throughout the process of testing many variables, we concluded that we have a good fit if each model iteration produces a similar solution to fit the data.